A Novel Aerial Reconfigurable Intelligent Surface-Assisted Channel Model Incorporating the Environmental Effects

Journal:	*IEEE Internet of Things Journal*
Manuscript ID	IoT-41126-2024
Manuscript Type:	Regular Article
Date Submitted by the Author:	22-Aug-2024
Complete List of Authors:	Wang, Zili; Shandong Normal University Bian, Ji; Shandong Normal University, School of Information Science and Engineering Wang, Cheng-Xiang; Southeast University, National Mobile Communications Research Laboratory; Purple Mountain Laboratories, Pervasive Communication Research Center Liu, Yu; Shandong University, School of Microelectronics Zhu, Qiuming; Nanjing University of Aeronautics and Astronautics, Eletronic and Information Engineering Mao, Kai; Nanjing University of Aeronautics and Astronautics, Eletronic and Information Engineering
Keywords:	Channel modeling, aerial reconfigurable intelligent surface (ARIS), unmanned aerial vehicle (UAV), UAV vibration, line-of-sight (LoS) probability

A Novel Aerial Reconfigurable Intelligent Surface-Assisted Channel Model Incorporating the Environmental Effects

Zili Wang, Ji Bian, *Member, IEEE*, Cheng-Xiang Wang, *Fellow, IEEE*, Yu Liu, *Member, IEEE*, Qiuming Zhu, *Senior Member, IEEE*, and Kai Mao, *Member, IEEE*

***Abstract*—This paper focuses on the aerial reconfigurable intelligent surface (ARIS) system, which is a novel transmission scheme where the RIS is attached to airborne platforms, e.g., drones. Compared to terrestrial RIS, ARIS offers advantages such as expanded coverage, increased deployment flexibility, and 360° panoramic signal reflection. However, the ARIS channel behavior and system performance are critically dependent on environmental factors. Specifically, drones may encounter random vibrations due to atmospheric turbulence or strong winds. Additionally, the direct paths between ground nodes and the drone could be blocked by buildings with a certain probability. This paper introduces a novel spatially consistent ARIS-assisted channel model designed to capture the impact of adverse weather conditions and ground building distribution on channel characteristics. Statistics including the spatial-temporal correlation function (ST-CF), Doppler power spectral density (PSD), average received signal power, and system achievable rate are derived. Results indicate that the environmental factors can significantly impact the statistics of the ARIS channel. Neglecting these factors may lead to an overestimation of the ST-CF and ARIS system performance.**

***Index Terms*—Channel modeling, aerial reconfigurable intelligent surface (ARIS), unmanned aerial vehicle (UAV), UAV vibration, line-of-sight (LoS) probability.**

I. Introduction

Reconfigurable intelligent surfaces (RISs) have garnered widespread interest from both researchers and industry professionals, owing to their potential to control electromagnetic waves [1]. RIS is a planar array consisting of numerous low-cost passive reflecting units (RUs), each capable of independently adjusting the phases and/or amplitudes of incoming electromagnetic waves in a programmable manner. This capability allows the reflected waves to be constructively combined to form a beam directed at a specific target or destructively aligned to reduce co-channel interference [2]. Leveraging these controllable and programmable features, RIS is envisioned as a transformative technology that can substantially enhance spectral efficiency, reduce energy consumption, and mitigate signal interference in future wireless networks [3]. In the development of more advanced systems, channel models are indispensable as they provide critical insights into real-world signal propagation behaviors [4], [5]. An accurate channel model should be able to capture the propagation environmental factors that affect channel characteristics. For emerging RIS systems, accurate and effective channel models are urgently needed.

A. Related Work

A distinct feature of RIS-assisted channels is the significant product-distance pathloss resulting from the cascaded channel structure. By treating the RIS as a continuous electromagnetic surface, a pathloss model for RIS-assisted channels was proposed in [6]. Under far-field free-space conditions, the pathloss was shown to vary proportionally with the square of the product of the transmitter (Tx)–RIS and RIS–receiver (Rx) distances. Additionally, the $\cos^q$ pattern was employed to characterize the non-isotropic radiation of RUs, resulting in a dependency between pathloss and RIS orientation [7]. Based on the free-space assumption, a similar pathloss model was proposed in [8], which can adapt to both near- and far-field transmission scenarios. The results were validated by measurement data collected in a microwave anechoic chamber. A different method was reported in [9] and [10], where the floating-intercept (FI) and close-in (CI) pathloss models were updated for RIS scenarios by fitting the models with measurement data. This approach allows the RIS pathloss models to be compatible with the classical fifth-generation (5G) pathloss models.

For small-scale fading, a straightforward modeling method is to treat the RIS as a virtual cluster and integrate it into conventional channel models. The key difference between a virtual cluster and a conventional one is that the phases of a conventional cluster are random, whereas the phases of a virtual cluster are programmable. This approach can efficiently model the RIS channel based on existing models. For example, in [11], a RIS was introduced aiming to enhance air-to-ground (A2G) communications. The scatterers surrounding the ground Rx were represented using a cylinder model. The

Manuscript received XX; revised XX; accepted XX. Date of publication XX. (*Corresponding author: Ji Bian.*)

Z. Wang and J. Bian are with the School of Information Science and Engineering, Shandong Normal University, Jinan, 250358, China (e-mail: wzili22@163.com; jibian@sdnu.edu.cn).

C.-X. Wang is with the National Mobile Communications Research Laboratory, School of Information Science and Engineering, Southeast University, Nanjing, 210096, China, and also with Purple Mountain Laboratories, Nanjing, 211111, China (e-mail: chxwang@seu.edu.cn).

Y. Liu is with School of Integrated Circuit, Shandong University, Jinan, 250101, China (e-mail: yuliu@sdu.edu.cn).

Qiuming Zhu and Kai Mao are with the Key Laboratory of Dynamic Cognitive System of Electromagnetic Spectrum Space, College of Electronic and Information Engineering, Nanjing University of Aeronautics and Astronautics, Nanjing 211106, China (e-mail: zhuqiuming@nuaa.edu.cn; maokai@nuaa.edu.cn)

impacts of unmanned aerial vehicle (UAV) altitude, trajectory, and RIS orientation on the channel statistics and capacity were analyzed. Similarly, a RIS model for A2G scenarios was reported in [12], where the propagation environment around the RIS and Rx was depicted using an elliptic-cylinder model. Additionally, a cylindrical model was adopted to depict the distribution of scatterers around the Rx. Furthermore, a double-RIS vehicle-to-vehicle (V2V) channel model was presented in [13], where transmissive RISs were deployed on vehicle windows. The scatterers in the vehicles and on the roadside environments were respectively depicted using two cylindrical models and an elliptic-cylinder model. The models presented in [11]–[13] consider that scatterers are located in regular shapes, which facilitate geometrical derivation and the acquisition of closed-form expressions for channel statistics. However, these models may be overly idealistic and less versatile in accurately capturing realistic scatterer distributions. In [14], the RIS was viewed as a virtual cluster and incorporated into a twin-cluster model. The impacts of the RU number, RU spacing, RIS orientation, and RIS shape on channel statistics were investigated. Similarly, in [15], a RIS-assisted high-speed train channel model was presented, in which transparent RISs were deployed on carriage windows to mitigate penetration loss. A twin-cluster model was used to depict the scatterers inside and outside the carriages. Moreover, a double-RIS A2G model was presented in [16]. The model was developed by summing the rays reflected by a single RIS, the rays successively reflected by two RISs, and the rays via conventional scatterers. The results demonstrated that the system utilizing double RISs outperforms the one with a single RIS. In general, the virtual cluster method makes the RIS channel model share a similar structure with the conventional channel model, thereby allowing a large number of channel parameters to be applied [17].

Apart from the virtual cluster method, another modeling approach is based on the dyadic backscatter principle. Specifically, the channel matrix is decomposed as $\mathbf{G\Phi H}+\mathbf{D}$, where $\mathbf{H}$ and $\mathbf{G}$ denote the channel matrices of Tx-RIS and RIS-Rx links, $\mathbf{\Phi}$ is a diagonal matrix containing the reflection coefficients of RUs, and $\mathbf{D}$ accounts for the channel matrix of the Tx-Rx link unaffected by the RIS. In [18], the Tx-RIS and RIS-Rx subchannels were described using Nakagami-m distributions. The bit error probability of the system was analyzed in terms of different Nakagami-m parameters. A more general model was reported in [19], where the RIS-assisted channel was divided into Tx-RIS, RIS-Rx, and Tx-Rx subchannels, each modeled by a 5G channel model [4]. The cluster evolution over the large RIS was simulated by a birth-death process. Generally, detailed modeling for the three subchannels introduces large model complexity. In [20], the three subchannels were modeled using 3GPP cluster-based models. For simplicity, the Rx and RIS were assumed to be closely located. Thus, the RIS-Rx channel was described by a pure line-of-sight (LoS) path, and the Tx-Rx and Tx-RIS subchannels were assumed to share the same cluster set.

In current research, RISs are primarily deployed on terrestrial structures, such as walls and building surfaces. This configuration limits the Tx and Rx to being on the identical side of the RIS, allowing signal reflections to occur in only half of the space. To address the intrinsic limitations of terrestrial RIS systems, a promising solution is the introduction of aerial RIS (ARIS), referring to a new transmission scheme in which the RIS is attached to an aerial platform, e.g., a UAV [21]–[23]. Due to its high mobility, ARIS offers advantages such as expanded coverage and increased deployment flexibility. Moreover, benefiting from its elevated position, ARIS can achieve 360° panoramic signal reflection. In [24], an ARIS-assisted channel model was introduced, utilizing a single cylinder model to capture the scatterer distribution around the Rx. The results demonstrated that real-time tunable RIS phases can substantially reduce multipath fading and Doppler effects. In [25], an ARIS-assisted channel model was introduced, demonstrating that its statistical properties can be represented as a combination of those of the individual subchannels and are heavily influenced by the RIS configuration.

B. Motivations

A realistic channel model should be able to faithfully reflect the impact of system configuration and propagation environments. Research shows that RIS can significantly improve system performance under non-LoS (NLoS) conditions. However, when a LoS link exists between the Tx and Rx, the performance gain offered by the RIS is minimal unless the RIS is extremely large [26]. To achieve remarkable system performance, existing research often assumes robust LoS connections in the Tx-RIS and RIS-Rx links while the direct link between the Tx and Rx is obstructed. In real-world scenarios, the presence of the LoS path can be described by a probability model, depending on factors including the locations of communication nodes and environmental conditions, e.g., the height and distribution density of ground buildings [27]. Additionally, without fixed facilities, UAVs may experience three-dimensional (3D) random wobbling due to wind and atmospheric turbulence. In the ARIS system, UAV wobbling can lead to phase misalignment in the reflected signals [28]. Neglecting these environmental factors may result in an overestimation of RIS system performance and lead to inaccurate outcomes in system design.

C. Contributions

Considering the aforementioned research gap, a 3D ARIS-aided channel model is proposed. The key contributions and innovations of this paper are outlined as follows:

- A 3D channel model for an ARIS-aided communication system is presented, taking into account both large-scale pathloss and small-scale fading. The proposed model can capture the effects of random UAV vibrations caused by adverse weather conditions. This is achieved by modeling the pitch, yaw, and roll angles of the UAV using stochastic sinusoidal processes. We demonstrate that UAV vibrations can introduce Doppler frequencies, resulting in phase misalignment of the signals reflected by the RIS. The effects of UAV vibration become more pronounced with the increase in carrier frequency.

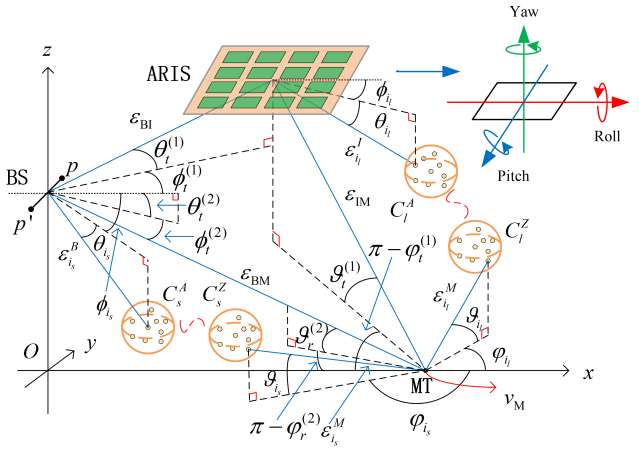

Fig. 1. A physical illustration of the proposed 3D ARIS auxiliary channel model.

- Unlike existing ARIS models, the proposed model assumes soft LoS states, which are spatially consistent random variables determined by factors such as carrier frequency, locations of communication nodes, as well as environmental factors including built-up land ratio, heights and distribution density of ground buildings. With suitable parameter adjustments, the proposed model can be adapted to various scenarios.
- The average received signal power is derived by taking into account key environmental factors. We demonstrate that adverse weather conditions and dense building environments significantly reduce the received signal power. Additionally, we prove that the law of squared power gain remains valid even in the presence of UAV vibrations. Further, we propose a method for predicting the optimal UAV height, which balances the trade-offs among LoS probability, pathloss, and effective apertures of RUs.
- Channel statistics, including spatial-temporal correlation function (ST-CF), Doppler power spectral density (PSD), and system achievable rate are derived. The impacts of system configuration and environmental factors on channel statistics are investigated, including the number of RUs, UAV altitude, amplitude and variation frequency of vibration angles, and the height and distribution of ground buildings. We demonstrate that compared to continuous reflection phases, 2-bit and 4-bit discrete phases do not cause significant degradation in achievable rates, even in environments with large UAV vibrations, verifying the practicability of ARIS systems.

The remainder of this paper is organized as follows. Section II describes the AIRS-aided channel model. Channel statistics are derived and analyzed in Section III. In Section IV, results and discussions are presented and the conclusions are drawn in Section V.

II. System Model

Fig. 1 illustrates a typical ARIS-assisted communication scenario, where the base station (BS) transmits signals to the mobile terminal (MT), with their locations defined as $(0, 0, z_{\mathrm{B}})$ and $(x_{\mathrm{M}}, 0, 0)$, respectively. The static BS is fitted with a uniform linear array with adjacent antenna spacings of δ_{B}. Additionally, $\gamma_{\mathrm{B}}^{\mathrm{A}}$ and $\gamma_{\mathrm{B}}^{\mathrm{E}}$ denote the azimuth and elevation angles of the BS array, respectively. The MT is fitted with a single omnidirectional antenna and moves in the horizontal plane at a speed of v_{M} and travels at an azimuth angle of α_{M}. To enhance coverage and link quality, panoramic signal reflections are achieved by mounting an RIS on a UAV, which is assumed to hover at the coordinates $(x_{\mathrm{U}}, y_{\mathrm{U}}, z_{\mathrm{U}})$. The RIS is composed of N RUs, where $N = N_x \times N_y$, N_x and N_y denote the numbers of columns and rows, respectively. The spacings between adjacent columns and rows of the RUs are δ_x and δ_y, respectively. Due to the elevated positions of the BS antennas and UAV, the subchannel between the BS and the RIS is modeled by a pure LoS path. However, the BS-MT and RIS-MT subchannels are composed of both LoS and NLoS paths due to the presence of scatterers. The key parameters of the proposed model are collected in Table I.

TABLE I
Summary of Key Parameter Definitions.

U_n	The nth reflecting unit in the RIS.
A_p^t	The pth BS antenna element.
$\varepsilon_{\mathrm{BM}}, \varepsilon_{\mathrm{IM}}, \varepsilon_{\mathrm{BI}}$	Distances of BS-MT, RIS-MT, and BS-RIS, respectively.
$\varepsilon_{\mathrm{BS},n}(t)$, $\varepsilon_{pn}(t), \varepsilon_{\mathrm{MT},n}(t)$	Distances of BS-U_n, A_p^t-U_n and U_n-MT at time t, respectively.
$\varepsilon_{i_l}^I, \varepsilon_{i_l}^n, \varepsilon_{i_l}^M$	Distances of RIS-C_l^A, U_n-C_l^A and C_l^Z-MT via the i_lth ray, respectively.
$\varepsilon_{i_s}^B, \varepsilon_{i_s}^M$	Distances of BS-C_s^A and C_s^Z-MT via the i_sth ray, respectively.
N_x, N_y	Numbers of columns and rows of RUs, respectively.
δ_x, δ_y	Spacings between adjacent columns and rows of RUs.
v_{M}, α_{M}	Speed and travel azimuth angle of the MT, respectively.
$\gamma_{\mathrm{B}}^{\mathrm{A}}$, $\gamma_{\mathrm{B}}^{\mathrm{E}}$	Azimuth and elevation angles of the BS array, respectively.
$\theta_t^{(1)}, \phi_t^{(1)}$ $(\vartheta_r^{(1)}, \varphi_r^{(1)})$	Elevation and azimuth angles from BS (MT) to RIS, respectively.
$\vartheta_r^{(2)}, \varphi_r^{(2)}$	Elevation and azimuth angles from MT to BS, respectively.
θ_{i_l}, ϕ_{i_l} $(\vartheta_{i_l}, \varphi_{i_l})$	Elevation and azimuth angles of departure (arrival) the i_lth ray in the RIS-MT subchannel, respectively.
θ_{i_s}, ϕ_{i_s} $(\vartheta_{i_s}, \varphi_{i_s})$	Elevation and azimuth angles of departure (arrival) of the i_sth ray in the BS-MT subchannel, respectively.

A. Frequency-Dependent LoS Probability Model

In realistic propagation environments, the LoS paths in BS-MT and RIS-MT channels could be obstructed by high buildings with certain probabilities, which depend on the environmental parameters α_0, β_0, and γ_0 [29]. Specifically, α_0 is the ratio of built-up land area to the total land area, β_0 denotes the building density (buildings/km^2), and γ_0 defines the average height of buildings. Here, the building heights follow the Rayleigh distribution, i.e., $p(h) = \frac{h}{\gamma_0^2} \exp\left(-\frac{h^2}{2\gamma_0^2}\right)$ [29]. Assuming that the buildings are located on a regular grid, the probability that the ith building does not obstruct the LoS

path is

$$p_i^{\mathrm{LoS}} = \int_0^{h_i} \frac{h}{\gamma_0^2} \exp\left(-\frac{h^2}{2\gamma_0^2}\right) \mathrm{d}h = 1 - \exp\left(-\frac{{h_i}^2}{2\gamma_0^2}\right) \quad (1)$$

where h_i represents the maximum height of the ith building that does not obstruct the LoS path, i.e.,

$$h_i = h_{tx} - \frac{\varepsilon_i (h_{tx} - h_{rx})}{\varepsilon_{2\mathrm{D}}} \quad (2)$$

where h_{rx} and h_{tx} denote the Tx and Rx heights, respectively, $\varepsilon_{2\mathrm{D}}$ is the horizontal distance between the Tx and Rx, $\varepsilon_i = \frac{(i+0.5)\varepsilon_{2\mathrm{D}}}{N_b}$ represents the horizontal distance between the ith building and the Tx, N_b is the average number of buildings located below the LoS path, and is given as $N_b = \left\lfloor \frac{\varepsilon_{2\mathrm{D}}\sqrt{\alpha_0 \beta_0}}{1000} \right\rfloor$, where $\lfloor \cdot \rfloor$ is the floor function. Thus, the probability of the LoS path exists if all the building lying in the propagation path are below the line connecting the Tx and Rx, i.e.,

$$p^{\mathrm{LoS}} = \prod_{i=0}^{N_b - 1} p_i^{\mathrm{LoS}}. \quad (3)$$

Under LoS propagation conditions, the energy of radio waves is not only concentrated along the optical path but is also distributed throughout the entire Fresnel zones, which are multiple confocal ellipsoidal regions centered around the LoS path. The radius of the nth Fresnel zone is approximated as $r_{n,i} \approx \sqrt{\frac{n\lambda d_{1,i} d_{2,i}}{d_{1,i} + d_{2,i}}}$, where $\lambda = \frac{c}{f_c}$ is the wavelength, f_c is the carrier frequency, and c is the speed of light [30]. Furthermore, $d_{1,i}$ and $d_{2,i}$ are the distances from the ith building to the Tx and Rx, respectively, and are calculated as

$$d_{1,i} = \frac{\varepsilon_i}{\varepsilon_{2\mathrm{D}}} \sqrt{\varepsilon_{2\mathrm{D}}^2 + (h_{tx} - h_{rx})^2} \quad (4)$$

$$d_{2,i} = (1 - \frac{\varepsilon_i}{\varepsilon_{2\mathrm{D}}}) \sqrt{\varepsilon_{2\mathrm{D}}^2 + (h_{tx} - h_{rx})^2}. \quad (5)$$

Typically, the LoS state requires the clearance of the first Fresnel zone. Thus, we have $r_{1,i} \approx \sqrt{\frac{d_{1,i} d_{2,i} \lambda}{d_{1,i} + d_{2,i}}}$, and (2) should be updated as

$$h_i = h_{tx} - \frac{\varepsilon_i (h_{tx} - h_{rx})}{\varepsilon_{2\mathrm{D}}} - \frac{r_{1,i}}{\cos\theta_{tr}} \quad (6)$$

where $\theta_{tr} = \arctan(\frac{h_{tx} - h_{rx}}{\varepsilon_{2\mathrm{D}}})$. By substituting (1) and (6) into (3), the LoS probability is expressed as

$$p^{\mathrm{LoS}}(\varepsilon_{2\mathrm{D}}, h_{tx}, h_{rx}) = \prod_{i=0}^{N_b - 1} \left[1 - \exp\Big(-\frac{\left(h_{tx} - \frac{\varepsilon_i (h_{tx} - h_{rx})}{\varepsilon_{2\mathrm{D}}} - \frac{r_{1,i}}{\cos\theta_{tr}}\right)^2}{2\gamma_0^2}\Big)\right]. \quad (7)$$

B. UAV Fluctuation Modeling

Due to the lack of fixed facilities, UAVs may experience random vibrations caused by atmospheric turbulence and adverse weather conditions. As depicted in Fig. 1, UAV vibrations can be described by the yaw angle $\zeta_{\mathrm{Y}}(t)$, pitch angle $\zeta_{\mathrm{P}}(t)$, and roll angle $\zeta_{\mathrm{R}}(t)$, respectively, which are modeled as the following sinusoidal processes [28]

$$\zeta_{\mathrm{Y}}(t) = \zeta_{\mathrm{Y}}(t_0) + \xi_{\mathrm{Y}} \sin(2\pi f_{\mathrm{Y}} t) \quad (8)$$

$$\zeta_{\mathrm{P}}(t) = \zeta_{\mathrm{P}}(t_0) + \xi_{\mathrm{P}} \sin(2\pi f_{\mathrm{P}} t) \quad (9)$$

$$\zeta_{\mathrm{R}}(t) = \zeta_{\mathrm{R}}(t_0) + \xi_{\mathrm{R}} \sin(2\pi f_{\mathrm{R}} t) \quad (10)$$

where $t_0 = 0$ indicates the initial time instant, ξ_{Y}, ξ_{P}, and ξ_{R} are independent random variables that describe the amplitudes of the yaw, pitch, and roll angles, respectively. Similarly, f_{Y}, f_{P}, and f_{R} represent the frequencies of the corresponding vibration angles following specific distributions. At initial time instant, the local coordinates of the nth RU, i.e., U_n, with respective to the center of the RIS can be described as $\mathbf{d}_n = [a_{n_x}, a_{n_y}, 0]^{\mathrm{T}}$, where $a_{n_x} = \frac{N_x - 2n_x + 1}{2}\delta_x$, $a_{n_y} = \frac{N_y - 2n_y + 1}{2}\delta_y$, $n_y = \left\lceil \frac{n}{N_x} \right\rceil$, $n_x = n - (n_y - 1)N_x$, $\lceil \cdot \rceil$ denotes the ceiling function. Thus, the local coordinates of U_n at time t can be calculated as

$$\begin{aligned} \mathbf{d}_n^{\mathrm{wob}}(t) &= \mathbf{R}_{\mathrm{Yaw}}(\zeta_{\mathrm{Y}}(t)) \mathbf{R}_{\mathrm{Pitch}}(\zeta_{\mathrm{P}}(t)) \mathbf{R}_{\mathrm{Roll}}(\zeta_{\mathrm{R}}(t)) \mathbf{d}_n \\ &= \begin{bmatrix} \cos\zeta_{\mathrm{Y}}(t) & -\sin\zeta_{\mathrm{Y}}(t) & 0 \\ \sin\zeta_{\mathrm{Y}}(t) & \cos\zeta_{\mathrm{Y}}(t) & 0 \\ 0 & 0 & 1 \end{bmatrix} \times \begin{bmatrix} \cos\zeta_{\mathrm{P}}(t) & 0 & \sin\zeta_{\mathrm{P}}(t) \\ 0 & 1 & 0 \\ -\sin\zeta_{\mathrm{P}}(t) & 0 & \cos\zeta_{\mathrm{P}}(t) \end{bmatrix} \\ &\times \begin{bmatrix} 1 & 0 & 0 \\ 0 & \cos\zeta_{\mathrm{R}}(t) & -\sin\zeta_{\mathrm{R}}(t) \\ 0 & \sin\zeta_{\mathrm{R}}(t) & \cos\zeta_{\mathrm{R}}(t) \end{bmatrix} \times \begin{bmatrix} a_{n_x} \\ a_{n_y} \\ 0 \end{bmatrix} \end{aligned} \quad (11)$$

where $\mathbf{R}_{\mathrm{Yaw}}(\zeta_{\mathrm{Y}}(t))$, $\mathbf{R}_{\mathrm{Pitch}}(\zeta_{\mathrm{P}}(t))$, and $\mathbf{R}_{\mathrm{Roll}}(\zeta_{\mathrm{R}}(t))$ are the rotation matrices of yaw, pitch, and roll angles, respectively.

C. Channel Impulse Response

The channel impulse response (CIR) between the pth ($p = 1, ..., P$) BS antenna, denoted as A_p^t, to MT, is written as

$$h_p(t) = h_p^{\mathrm{RIS}}(t) + h_p^{\mathrm{env}}(t) \quad (12)$$

where $h_p^{\mathrm{RIS}}(t)$ represents the CIR of the controllable channel via the RIS, while $h_p^{\mathrm{env}}(t)$ is the CIR of the uncontrollable channel which is not affected by the RIS.

1) Controllable Channel: The CIR of the controllable channel is composed of the virtual LoS (VLoS) and NLoS components, i.e.,

$$h_p^{\mathrm{RIS}}(t) = \bar{h}_p^{\mathrm{RIS}}(t) + \tilde{h}_p^{\mathrm{RIS}}(t) \quad (13)$$

where the $\bar{h}_p^{\mathrm{RIS}}(t)$ and $\tilde{h}_p^{\mathrm{RIS}}(t)$ refer to the CIR of the BS-RIS-MT and BS-RIS-$\mathcal{C}_L$-MT links, respectively, $\mathcal{C}_L$ indicates the cluster set in the controllable channel. The CIR of the VLoS component can be written as

$$\begin{aligned} \bar{h}_p^{\mathrm{RIS}}(t) = \frac{4\pi}{\lambda^2} \delta_x \delta_y \sqrt{\frac{K_1 \mathrm{PL}_t^{-1} \mathrm{PL}_r^{-1}}{1 + K_1}} \\ \times \sqrt{G_t G_r \cos\varsigma_t \cos\varsigma_r} \sum_{n=1}^{N} e^{j\psi_n(t)} \\ \times e^{j\chi_{pn}(t)} \cdot e^{j\chi_{\mathrm{MT},n}(t)} \end{aligned} \quad (14)$$

where ψ_n is the phase shift of U_n, G_t and G_r are the gains of transmit and receive antennas, respectively, K_1 accounts for the power ratio between the VLoS and NLoS components, $\cos\varsigma_t = \langle \mathbf{n}, \mathbf{r}_{\mathrm{in}} / \|\mathbf{r}_{\mathrm{in}}\| \rangle$, $\cos\varsigma_r = \langle \mathbf{n}, \mathbf{r}_{\mathrm{out}} / \|\mathbf{r}_{\mathrm{out}}\| \rangle$, $\langle \cdot, \cdot \rangle$ denotes the inner product, $\mathbf{r}_{\mathrm{in}} = [-x_{\mathrm{U}}, -y_{\mathrm{U}}, z_{\mathrm{B}} - z_{\mathrm{U}}]^{\mathrm{T}}$ and $\mathbf{r}_{\mathrm{out}} = [x_{\mathrm{M}} - x_{\mathrm{U}}, -y_{\mathrm{U}}, -z_{\mathrm{U}}]^{\mathrm{T}}$ account for the vectors from the RIS to BS and MT, respectively. Besides, $\mathbf{n} = [0, 0, -1]^{\mathrm{T}}$ is the unit normal vector representing the broadside of the RIS. Furthermore, $\chi_{pn}(t) = \frac{2\pi\varepsilon_{pn}(t)}{\lambda}$ represents the phase rotation

of the wave due to the travel distance from A_p^t to U_n. Similarly, $\chi_{\mathrm{MT},n}(t) = \frac{2\pi\varepsilon_{\mathrm{MT},n}(t)}{\lambda}$ accounts for the phase rotation of the wave due to the travel distance from U_n to MT, $\varepsilon_{pn}(t)$ and $\varepsilon_{\mathrm{MT},n}(t)$ are the distances of A_p^t-U_n and U_n-MT, respectively. In addition, $\mathrm{PL}_t = \mathrm{PL}^{\mathrm{CI}}(f_c, \varepsilon_{\mathrm{BI}})$ and $\mathrm{PL}_r = \mathrm{PL}^{\mathrm{CI}}(f_c, \varepsilon_{\mathrm{IM}})$ are the pathloss of BS-RIS and RIS-MT link, respectively, where $\varepsilon_{\mathrm{BI}} = \|\mathbf{r}_{\mathrm{in}}\|$ and $\varepsilon_{\mathrm{IM}} = \|\mathbf{r}_{\mathrm{out}}\|$. Here, the CI pathloss model is adopted, which was widely used in evaluating aerial communication systems, i.e., [31]

$$\mathrm{PL}^{\mathrm{CI}}(f_c, d)[\mathrm{dB}] = 20\log_{10}(\frac{4\pi f_c}{c}) + 10n_{\mathrm{PLE}}\log_{10}(d) \quad (15)$$

where n_{PLE} is the pathloss exponent (PLE). The CIR in (14) is derived in Appendix A.

Proposition 1: The travel distances from the BS array center to U_n at time t can be calculated as

$$\begin{aligned}\varepsilon_{\mathrm{BS},n}(t) \approx{}& \varepsilon_{\mathrm{BI}} + a_{n_x}\cdot\cos\theta_t^{(1)}\cdot\cos\phi_t^{(1)} \\ &+ a_{n_y}\cdot\cos\theta_t^{(1)}\cdot\sin\phi_t^{(1)} \\ &+ \zeta_{\mathrm{Y}}(t)\cdot\bar{X}_{\mathrm{Y},n}^B - \zeta_{\mathrm{P}}(t)\cdot\bar{X}_{\mathrm{P},n}^B + \zeta_{\mathrm{R}}(t)\cdot\bar{X}_{\mathrm{R},n}^B \quad (16)\end{aligned}$$

where $\bar{X}_{\mathrm{Y},n}^B = a_{n_x}\cos\theta_t^{(1)}\sin\phi_t^{(1)} - a_{n_y}\cos\theta_t^{(1)}\cos\phi_t^{(1)}$, $\bar{X}_{\mathrm{P},n}^B = a_{n_x}\sin\theta_t^{(1)}$, and $\bar{X}_{\mathrm{R},n}^B = a_{n_y}\sin\theta_t^{(1)}$. In addition, $\phi_t^{(1)}$ and $\theta_t^{(1)}$ are the azimuth angle of departure (AoD) and elevation angle of departure (EoD) of the waves impinging on the RIS, and can be obtained as $\phi_t^{(1)} = \mathrm{atan2}(y_{\mathrm{U}}, x_{\mathrm{U}})$, $\theta_t^{(1)} = \arctan(\frac{z_{\mathrm{U}}-z_{\mathrm{B}}}{\sqrt{x_{\mathrm{U}}^2+y_{\mathrm{U}}^2}})$, where atan2$(\cdot)$ is the four-quadrant inverse tangent function.

Proof: See Appendix B. ■

Proposition 2: The travel distances from U_n to the MT array center at time t can be calculated as

$$\begin{aligned}\varepsilon_{\mathrm{MT},n}(t) \approx{}& \varepsilon_{\mathrm{IM}} + a_{n_x}\cdot\cos\vartheta_r^{(1)}\cdot\cos\varphi_r^{(1)} \\ &+ a_{n_y}\cdot\cos\vartheta_r^{(1)}\cdot\sin\varphi_r^{(1)} \\ &- \frac{v_{\mathrm{M}}t}{\lambda}\cdot\cos\vartheta_r^{(1)}\cdot\cos(\varphi_r^{(1)}-\alpha_{\mathrm{M}}) \\ &+ \zeta_{\mathrm{Y}}(t)\cdot\bar{X}_{\mathrm{Y},n}^M - \zeta_{\mathrm{P}}(t)\cdot\bar{X}_{\mathrm{P},n}^M + \zeta_{\mathrm{R}}(t)\cdot\bar{X}_{\mathrm{R},n}^M \quad (17)\end{aligned}$$

where $\bar{X}_{\mathrm{Y},n}^M = a_{n_x}\cos\vartheta_r^{(1)}\sin\varphi_r^{(1)} - a_{n_y}\cos\vartheta_r^{(1)}\cos\varphi_r^{(1)}$, $\bar{X}_{\mathrm{P},n}^M = a_{n_x}\sin\vartheta_r^{(1)}$, $\bar{X}_{\mathrm{R},n}^M = a_{n_y}\sin\vartheta_r^{(1)}$. In addition, $\varphi_r^{(1)}$ and $\vartheta_r^{(1)}$ are the azimuth angle of arrival (AoA) and elevation angle of arrival (EoA) of the waves reflected by the ARIS, and can be obtained as $\varphi_r^{(1)} = \mathrm{atan2}(y_{\mathrm{U}}, x_{\mathrm{U}} - x_{\mathrm{M}})$ and $\vartheta_r^{(1)} = \arctan(\frac{z_{\mathrm{U}}}{\sqrt{(x_{\mathrm{U}}-x_{\mathrm{M}})^2+y_{\mathrm{U}}^2}})$. The proof of (17) follows a similar procedure to that of (16) and is omitted here due to space constraints.

Based on the plane wavefront assumption, the distance from A_p^t to U_n can be written as

$$\begin{aligned}\varepsilon_{pn}(t) \approx{}& \varepsilon_{\mathrm{BS},n}(t) + \Delta_p\cdot[\cos\theta_t^{(1)}\cdot\cos\gamma_{\mathrm{B}}^{\mathrm{E}}\cdot\cos(\phi_t^{(1)}-\gamma_{\mathrm{B}}^{\mathrm{A}}) \\ &+ \sin\theta_t^{(1)}\cdot\sin\gamma_{\mathrm{B}}^{\mathrm{E}}] \quad (18)\end{aligned}$$

where $\Delta_p = \frac{P-2p+1}{2}\delta_{\mathrm{B}}$. By substituting (16)–(18) into (14), $\bar{h}_p^{\mathrm{RIS}}(t)$ can be rewritten as

$$\begin{aligned}\bar{h}_p^{\mathrm{RIS}}(t) = {}& \frac{4\pi}{\lambda^2}\delta_x\delta_y\sqrt{\frac{K_1\mathrm{PL}_t^{-1}\mathrm{PL}_r^{-1}}{1+K_1}} \\ &\times\sqrt{G_tG_r\cos\varsigma_t\cos\varsigma_r}\sum_{n=1}^{N}e^{j\psi_n(t)}e^{j\frac{2\pi}{\lambda}(\varepsilon_{\mathrm{IM}}+\varepsilon_{\mathrm{BI}})} \\ &\times e^{j\frac{2\pi}{\lambda}\Delta_p[\cos\theta_t^{(1)}\cos\gamma_{\mathrm{B}}^{\mathrm{E}}\cos(\phi_t^{(1)}-\gamma_{\mathrm{B}}^{\mathrm{A}})+\sin\theta_t^{(1)}\sin\gamma_{\mathrm{B}}^{\mathrm{E}}]} \\ &\times e^{j\frac{2\pi}{\lambda}a_{n_x}[\cos\theta_t^{(1)}\cos\phi_t^{(1)}+\cos\vartheta_r^{(1)}\cos\varphi_r^{(1)}]} \\ &\times e^{j\frac{2\pi}{\lambda}a_{n_y}[\cos\theta_t^{(1)}\sin\phi_t^{(1)}+\cos\vartheta_r^{(1)}\sin\varphi_r^{(1)}]} \\ &\times e^{j\frac{2\pi}{\lambda}[\zeta_{\mathrm{Y}}(t)\bar{X}_{\mathrm{Y},n}+\zeta_{\mathrm{P}}(t)\bar{X}_{\mathrm{P},n}+\zeta_{\mathrm{R}}(t)\bar{X}_{\mathrm{R},n}]}\cdot e^{j2\pi\nu_{M,L}t} \quad (19)\end{aligned}$$

where $\bar{X}_{\mathrm{Y},n} = \bar{X}_{\mathrm{Y},n}^B + \bar{X}_{\mathrm{Y},n}^M$, $\bar{X}_{\mathrm{P},n} = -\bar{X}_{\mathrm{P},n}^B - \bar{X}_{\mathrm{P},n}^M$, and $\bar{X}_{\mathrm{R},n} = \bar{X}_{\mathrm{R},n}^B + \bar{X}_{\mathrm{R},n}^M$, $\nu_{M,L} = -\frac{v_{\mathrm{M}}}{\lambda}\cdot\cos\vartheta_r^{(1)}\cdot\cos(\varphi_r^{(1)} - \alpha_{\mathrm{M}})$. Equation (19) yields deep insights of how the phase of $\bar{h}_p^{\mathrm{RIS}}$ changes over time. The phase variation stems from the following components

- $\psi_n(t)$ is the phase shift induced by U_n.
- $\frac{2\pi}{\lambda}(\varepsilon_{\mathrm{BI}} + \varepsilon_{\mathrm{IM}})$ is the phase shift caused by the travel distance of BS-RIS and RIS-MT at initial time instant.
- $\frac{2\pi}{\lambda}\Delta_p[\cos\theta_t^{(1)}\cos\gamma_{\mathrm{B}}^{\mathrm{E}}\cos(\phi_t^{(1)}-\gamma_{\mathrm{B}}^{\mathrm{A}}) + \sin\theta_t^{(1)}\sin\gamma_{\mathrm{B}}^{\mathrm{E}}]$ is the phase shift caused by the relative locations of antennas in the BS arrays.
- $\frac{2\pi}{\lambda}a_{n_x}[\cos\theta_t^{(1)}\cos\phi_t^{(1)} + \cos\vartheta_r^{(1)}\cos\varphi_r^{(1)}]$ and $\frac{2\pi}{\lambda}a_{n_y}[\cos\theta_t^{(1)}\sin\phi_t^{(1)} + \cos\vartheta_r^{(1)}\sin\varphi_r^{(1)}]$ are the phase shifts caused by the relative locations of RUs along the x and y axes, respectively.
- $2\pi\nu_{M,L}\cdot t$ is the phase shift resulting from the movement of MT.
- $\frac{2\pi}{\lambda}[\zeta_{\mathrm{Y}}(t)\bar{X}_{\mathrm{Y},n} + \zeta_{\mathrm{P}}(t)\bar{X}_{\mathrm{P},n} + \zeta_{\mathrm{R}}(t)\bar{X}_{\mathrm{R},n}]$ is the phase shift caused by the random vibration of UAV. Defining $\hat{\theta}(t) = \frac{2\pi}{\lambda}[\zeta_{\mathrm{Y}}(t)\bar{X}_{\mathrm{Y},n} + \zeta_{\mathrm{P}}(t)\bar{X}_{\mathrm{P},n} + \zeta_{\mathrm{R}}(t)\bar{X}_{\mathrm{R},n}]$, the UAV fluctuations introduce an effective Doppler shift, i.e.,

$$\begin{aligned}\frac{1}{2\pi}\frac{\mathrm{d}\hat{\theta}(t)}{\mathrm{d}t} = {}& \frac{2\pi}{\lambda}f_{\mathrm{Y}}\cdot\xi_{\mathrm{Y}}\cdot\bar{X}_{\mathrm{Y},n}\cdot\cos(2\pi f_{\mathrm{Y}}t) \\ &+ \frac{2\pi}{\lambda}f_{\mathrm{P}}\cdot\xi_{\mathrm{P}}\cdot\bar{X}_{\mathrm{P},n}\cdot\cos(2\pi f_{\mathrm{P}}t) \\ &+ \frac{2\pi}{\lambda}f_{\mathrm{R}}\cdot\xi_{\mathrm{R}}\cdot\bar{X}_{\mathrm{R},n}\cdot\cos(2\pi f_{\mathrm{R}}t). \quad (20)\end{aligned}$$

By substituting (8)–(10) into (19) and applying Jacobi-Anger expansion, $\bar{h}_p^{\mathrm{RIS}}$ can be expanded as

$$\begin{aligned}\bar{h}_p^{\mathrm{RIS}}(t) = {}& \frac{4\pi}{\lambda^2}\delta_x\delta_y\sqrt{\frac{K_1\mathrm{PL}_t^{-1}\mathrm{PL}_r^{-1}}{1+K_1}} \\ &\times\sqrt{G_tG_r\cos\varsigma_t\cos\varsigma_r}\sum_{n=1}^{N}e^{j\psi_n(t)}e^{j\varpi_{\mathrm{MT},pn}(t)} \\ &\times e^{j\frac{2\pi}{\lambda}[\zeta_{\mathrm{Y}}(t_0)\bar{X}_{\mathrm{Y},n}+\zeta_{\mathrm{P}}(t_0)\bar{X}_{\mathrm{P},n}+\zeta_{\mathrm{R}}(t_0)\bar{X}_{\mathrm{R},n}]} \\ &\times\sum_{k_1=-\infty}^{\infty}\sum_{k_2=-\infty}^{\infty}\sum_{k_3=-\infty}^{\infty}\Bigg[J_{k_1}\left(\frac{2\pi}{\lambda}\cdot\bar{X}_{\mathrm{Y},n}\cdot\xi_{\mathrm{Y}}\right) \\ &\times J_{k_2}\left(\frac{2\pi}{\lambda}\cdot\bar{X}_{\mathrm{P},n}\cdot\xi_{\mathrm{P}}\right)\cdot J_{k_3}\left(\frac{2\pi}{\lambda}\cdot\bar{X}_{\mathrm{R},n}\cdot\xi_{\mathrm{R}}\right) \\ &\times e^{j2\pi(k_1f_{\mathrm{Y}}+k_2f_{\mathrm{P}}+k_3f_{\mathrm{R}})t}\Bigg] \quad (21)\end{aligned}$$

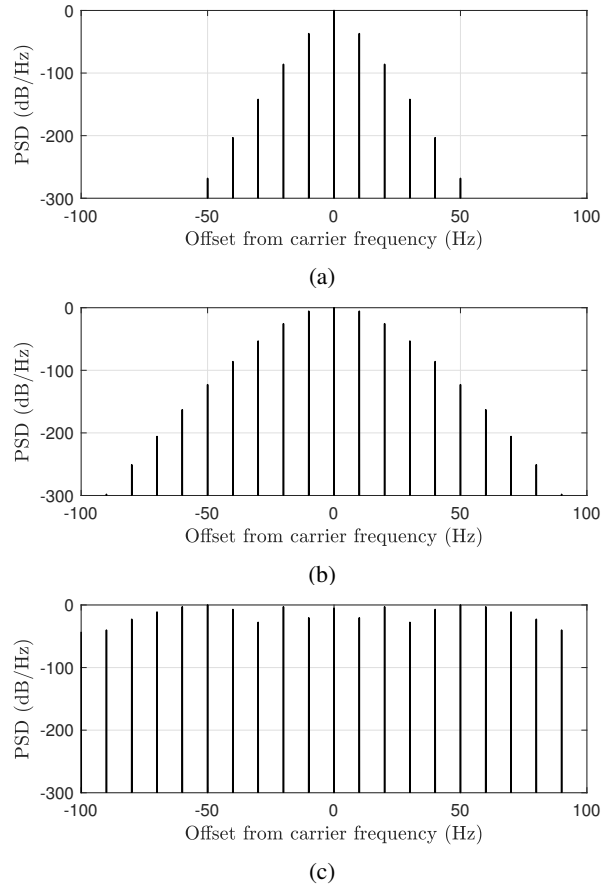

Fig. 2. The impacts of UAV fluctuations on the PSD of VLoS component with (a) $\zeta_{\mathrm{X}} = 0.1^\circ$ and $f_c = 5$ GHz, (b) $\zeta_{\mathrm{X}} = 0.5^\circ$ and $f_c = 5$ GHz, and (c) $\zeta_{\mathrm{X}} = 0.5^\circ$ and $f_c = 28$ GHz, where $\mathrm{X} \in \{\mathrm{Y}, \mathrm{P}, \mathrm{R}\}$.

where $\varpi_{\mathrm{MT},pn}(t)$ denotes the phase shift of the wave between A_p^t and MT via U_n that eliminating the effect of UAV fluctuations, $J_k(\cdot)$ is the kth order Bessel function of the first kind. Equation (21) shows that the yaw, pitch, and roll vibration angles introduce a series of lower and upper sidebands at frequency offsets $k_1 f_{\mathrm{Y}}$, $k_2 f_{\mathrm{P}}$, and $k_3 f_{\mathrm{R}}$, respectively. The Bessel functions depicts the power of the harmonic components, which depend on the wavelength, amplitudes of vibration angles, and the directions of impinging and reflected rays. To further illustrate this, the PSD of the VLoS component is shown in Fig. 2. For clarity, we set $v_{\mathrm{M}} = 0$ m/s, $f_{\mathrm{Y}} = f_{\mathrm{P}} = f_{\mathrm{R}} = 10$ Hz, and phases of RUs are set as constant values. It is observed that the sidebands are symmetrically distributed around the carrier frequency at integer multiples of the vibration frequencies. In Fig. 2(a), the power of the sidebands decreases rapidly with the increase in frequency offset. However, in Fig. 2(b), the power of the sidebands reduces relatively slowly due to the increase in vibration angle amplitudes. The largest sideband power is observed in Fig. 2(c) by further increasing the carrier frequency.

Similarly, the CIR of BS-RIS-$\mathcal{C}_L$-MT subchannel can be written as

$$\tilde{h}_p^{\mathrm{RIS}}(t) = \frac{4\pi}{\lambda^2}\delta_x\delta_y\sqrt{\frac{\mathrm{PL}_t^{-1}\mathrm{PL}_r^{-1}G_tG_r}{1+K_1}} \times \sum_{n=1}^{N}\sum_{l=1}^{L}\sum_{i_l=1}^{I_l}\sqrt{\frac{P_l}{I_l}\cos\varsigma_t\cos\varsigma_{r,i_l}} \times e^{j\psi_n(t)}\cdot e^{j\epsilon_{i_l}}\cdot e^{j(\chi_{pn}(t)+\chi_{i_l}^n(t)+\hat{\chi}_{i_l}+\chi_{i_l}^M(t))} \quad (22)$$

where L is the number of clusters in the controllable channel, I_l is the number of rays in the lth cluster, ς_{r,i_l} denotes the angle of the i_lth ray in the lth cluster reflected by the RIS with respect to the RIS broadside, and is determined as $\cos\varsigma_{r,i_l} = \langle \mathbf{n}, \mathbf{r}_{\mathrm{out},i_l}/\|\mathbf{r}_{\mathrm{out},i_l}\|\rangle$, $\mathbf{r}_{\mathrm{out},i_l} = [\cos\theta_{i_l}\cos\phi_{i_l}, \cos\theta_{i_l}\sin\phi_{i_l}, \sin\theta_{i_l}]^{\mathrm{T}}$. Besides, P_l are the cluster powers satisfying $\sum_{l=1}^{L} P_l = 1$, $\epsilon_{i_l} \sim \mathrm{U}(0, 2\pi)$ is the initial random phase, $\chi_{i_l}^n(t) = \frac{2\pi\varepsilon_{i_l}^n(t)}{\lambda}$, $\chi_{i_l}^M(t) = \frac{2\pi\varepsilon_{i_l}^M(t)}{\lambda}$, $\hat{\chi}_{i_l}(t) = \frac{2\pi\hat{\varepsilon}_{i_l}(t)}{\lambda}$, where $\varepsilon_{i_l}^n(t)$, $\varepsilon_{i_l}^M(t)$, and $\hat{\varepsilon}_{i_l}$ are travel distances U_n-C_l^A, C_l^Z-MT, and C_l^A-C_l^Z, respectively, C_l^A and C_l^Z stand for the first and last bounce clusters in the lth path, respectively. Following a similar method in (18), the travel distance $\varepsilon_{i_l}^n(t)$ can be written as

$$\varepsilon_{i_l}^n(t) \approx \varepsilon_{i_l}^I + a_{n_x}\cdot\cos\theta_{i_l}\cdot\cos\phi_{i_l} + a_{n_y}\cdot\cos\theta_{i_l}\cdot\sin\phi_{i_l} + \zeta_{\mathrm{Y}}(t)\cdot\tilde{X}_{\mathrm{Y},n,i_l}^A - \zeta_{\mathrm{P}}(t)\cdot\tilde{X}_{\mathrm{P},n,i_l}^A + \zeta_{\mathrm{R}}(t)\cdot\tilde{X}_{\mathrm{R},n,i_l}^A \quad (23)$$

where $\tilde{X}_{\mathrm{Y},n,i_l}^A = a_{n_x}\cos\theta_{i_l}\sin\phi_{i_l} - a_{n_y}\cos\theta_{i_l}\cos\phi_{i_l}$, $\tilde{X}_{\mathrm{P},n,i_l}^A = a_{n_x}\sin\theta_{i_l}$, $\tilde{X}_{\mathrm{R},n,i_l}^A = a_{n_y}\sin\theta_{i_l}$, θ_{i_l} and ϕ_{i_l} are EoD and AoD from RIS to C_l^A via the i_l ray, respectively, ϑ_{i_l} and φ_{i_l} are EoA and AoA from C_l^Z to MT via the i_lth ray, respectively, $\nu_{M,N} = -\frac{v_{\mathrm{M}}}{\lambda}\cdot\cos\vartheta_{i_l}\cdot\cos(\varphi_{i_l}-\alpha_{\mathrm{M}})$ is the Doppler shift in the NLoS component stemming from the moving MT, $\varepsilon_{i_l}^I$ is the distance between RIS center and C_l^A. By substituting (16), (18), and (23) into (22), $\tilde{h}_p^{\mathrm{RIS}}(t)$ can be expressed as

$$\begin{aligned}\tilde{h}_p^{\mathrm{RIS}}(t) = {}& \frac{4\pi}{\lambda^2}\delta_x\delta_y\sqrt{\frac{\mathrm{PL}_t^{-1}\mathrm{PL}_r^{-1}G_tG_r}{1+K_1}} \times \sum_{l=1}^{L}\sum_{i_l=1}^{I_l}\sum_{n=1}^{N}\sqrt{\frac{P_l}{I_l}\cos\varsigma_t\cos\varsigma_{r,i_l}} \\ & \times e^{j\frac{2\pi}{\lambda}(\varepsilon_{\mathrm{BI}}+\varepsilon_{i_l}^I+\varepsilon_{i_l}^M+\hat{\varepsilon}_{i_l})}\cdot e^{j\psi_n(t)}\cdot e^{j\epsilon_{i_l}} \\ & \times e^{j\frac{2\pi}{\lambda}\Delta_p[\cos\theta_t^{(1)}\cos\gamma_{\mathrm{B}}^{\mathrm{E}}\cos(\phi_t^{(1)}-\gamma_{\mathrm{B}}^{\mathrm{A}})+\sin\theta_t^{(1)}\sin\gamma_{\mathrm{B}}^{\mathrm{E}}]} \\ & \times e^{j\frac{2\pi}{\lambda}a_{n_x}[\cos\theta_t^{(1)}\cos\phi_t^{(1)}+\cos\theta_{i_l}\cos\phi_{i_l}]} \\ & \times e^{j\frac{2\pi}{\lambda}a_{n_y}[\cos\theta_t^{(1)}\sin\phi_t^{(1)}+\cos\theta_{i_l}\sin\phi_{i_l}]} \\ & \times e^{j\frac{2\pi}{\lambda}[\zeta_{\mathrm{Y}}(t)\tilde{X}_{\mathrm{Y},n,i_l}+\zeta_{\mathrm{P}}(t)\tilde{X}_{\mathrm{P},n,i_l}+\zeta_{\mathrm{R}}(t)\tilde{X}_{\mathrm{R},n,i_l}]}\cdot e^{j2\pi\nu_{M,N}t}\end{aligned} \quad (24)$$

where $\tilde{X}_{\mathrm{Y},n,i_l} = \bar{X}_{\mathrm{Y},n}^B + \tilde{X}_{\mathrm{Y},n,i_l}^A$, $\tilde{X}_{\mathrm{P},n,i_l} = -\bar{X}_{\mathrm{P},n}^B - \tilde{X}_{\mathrm{P},n,i_l}^A$, and $\tilde{X}_{\mathrm{R},n,i_l} = \bar{X}_{\mathrm{R},n}^B + \tilde{X}_{\mathrm{R},n,i_l}^A$.

2) Uncontrollable Channel: The CIR of the uncontrollable channel eliminating the RIS effect can be written as

$$h_p^{\mathrm{env}}(t) = \bar{h}_p^{\mathrm{env}}(t) + \tilde{h}_p^{\mathrm{env}}(t) \quad (25)$$

where $\bar{h}_p^{\text{env}}(t)$ and $\tilde{h}_p^{\text{env}}(t)$ represent the CIR of BS-MT and BS-$\mathcal{C}_S$-MT links, respectively, $\mathcal{C}_S$ indicates the cluster set in the uncontrollable channel. The LoS component can be written as

$$\begin{aligned}\bar{h}_p^{\text{env}}(t) = &\sqrt{\frac{K_2 \cdot \text{PL}_{\text{env}}^{-1}}{1+K_2}} \cdot e^{j\frac{2\pi}{\lambda}\varepsilon_{\text{BM}}} \\ &\times e^{j\frac{2\pi}{\lambda}\Delta_p[\sin\theta_t^{(2)}\sin\gamma_{\text{B}}^{\text{E}}+\cos\theta_t^{(2)}\cos\gamma_{\text{B}}^{\text{E}}\cos(\phi_t^{(2)}-\gamma_{\text{B}}^{\text{A}})]} \\ &\times e^{-j\frac{2\pi}{\lambda}v_{\text{M}}t[\cos\vartheta_r^{(2)}\cos(\varphi_r^{(2)}-\alpha_{\text{M}})]} \end{aligned} \tag{26}$$

where $\text{PL}_{\text{env}} = \text{PL}^{\text{CI}}(f_c, \varepsilon_{\text{BM}})$, $\varepsilon_{\text{BM}} = \sqrt{z_{\text{B}}^2 + x_{\text{M}}^2}$, $\theta_t^{(2)}$ and $\phi_t^{(2)}$ are the EoD and AoD of the LoS path, respectively, $\vartheta_r^{(2)}$ and $\varphi_r^{(2)}$ are the EoA and AoA of the LoS path, respectively, which are obtained as $\phi_t^{(2)} = 0$, $\varphi_r^{(2)} = \pi$, $\theta_t^{(2)} = -\arctan(\frac{z_{\text{B}}}{x_{\text{M}}})$, $\vartheta_r^{(2)} = -\theta_t^{(2)}$. The CIR of the NLoS component of the uncontrollable channel is calculted as

$$\begin{aligned}\tilde{h}_p^{\text{env}}(t) = &\sqrt{\frac{\text{PL}_{\text{env}}^{-1}}{1+K_2}} \cdot \sum_{s=1}^{\text{S}}\sum_{i_s=1}^{I_s}\sqrt{\frac{P_s}{I_s}} \\ &\times e^{j\epsilon_{i_s}} \cdot e^{j\frac{2\pi}{\lambda}(\varepsilon_{i_s}^B+\varepsilon_{i_s}^M+\hat{\varepsilon}_{i_s})} \\ &\times e^{j\frac{2\pi}{\lambda}\Delta_p[\cos\theta_{i_s}\cos\gamma_{\text{B}}^{\text{E}}\cos(\phi_{i_s}-\gamma_{\text{B}}^{\text{A}})+\sin\theta_{i_s}\sin\gamma_{\text{B}}^{\text{E}}]} \\ &\times e^{-j\frac{2\pi}{\lambda}v_{\text{M}}t[\cos\vartheta_{i_s}\cos(\varphi_{i_s}-\alpha_{\text{M}})]} \end{aligned} \tag{27}$$

where S is the number of clusters in the uncontrollable channel, I_s denotes the number of rays within the sth cluster, $\varepsilon_{i_s}^B$, $\varepsilon_{i_s}^M$, and $\hat{\varepsilon}_{i_s}$ represents the travel distance BS-C_s^A, C_s^Z-MT, and C_s^A-C_s^Z, respectively, C_s^A and C_s^Z denote the first and the last bounce clusters in the sth path, respectively, $\epsilon_{i_s} \sim \text{U}(0, 2\pi)$ is initial random phase, P_s are the cluster powers fulfilling $\sum_{s=1}^{S} P_s = 1$. Furthermore, θ_{i_s}, ϕ_{i_s}, ϑ_{i_s}, and φ_{i_s} stand for the EoD, AoD, EoA, and AoA of the i_sth ray, respectively.

D. Spatially Consistent ARIS Channel with Soft LoS State

In the BS-RIS-MT subchannel, the VLoS component may be blocked by buildings, with the probability of blockage varying continuously based on the positions of the UAV and MT. To achieve a smooth transition of channel characteristics over space, the soft VLoS state is introduced as follows [17]

$$\text{LoS}_{\text{soft}}^{\text{RIS}} = \frac{1}{2} + \frac{1}{\pi}\arctan(\sqrt{\frac{20}{\lambda}}(G + F_{\text{RIS}})) \tag{28}$$

where G is a spatially consistent Gaussian random variable with correlation distance, F_{RIS} is given as

$$F_{\text{RIS}} = \sqrt{2}\text{erf}^{-1}(2p_{\text{RIS}}^{\text{LoS}}(\varepsilon_{\text{IM}}^{2D}, z_{\text{U}}) - 1) \tag{29}$$

where $\text{erf}^{-1}(\cdot)$ denotes the inverse error function, $\varepsilon_{\text{IM}}^{2D} = \sqrt{(x_{\text{M}} - x_{\text{U}})^2 + y_{\text{U}}^2}$ is the horizontal distance between ARIS and MT. Note that the VLoS path exists only when both the LoS path between the BS and ARIS and the LoS path between the ARIS and MT are not blocked. Note that the parameters $z_{\text{M}} = 0$ and is omitted for brevity. Since the BS antennas and ARIS are relatively high, it is assumed that the LoS path in the BS-ARIS link always exists. Thus, the VLoS probability only depends on the LoS state of the ARIS-MT link, i.e., $p_{\text{RIS}}^{\text{LoS}}(\varepsilon_{\text{IM}}^{2D}, z_{\text{U}})$. The spatially consistent controllable channel with soft LoS state can be obtained as

$$\begin{aligned}h_p^{\text{RIS}}(t) = &h_{\text{LoS},p}^{\text{RIS}}(t) \cdot \text{LoS}_{\text{soft}}^{\text{RIS}} \\ &+ h_{\text{NLoS},p}^{\text{RIS}}(t) \cdot \sqrt{1 - (\text{LoS}_{\text{soft}}^{\text{RIS}})^2} \end{aligned} \tag{30}$$

where $h_{\text{LoS},p}^{\text{RIS}}(t)$ and $h_{\text{NLoS},p}^{\text{RIS}}(t)$ are the CIRs of the controllable channel generated by the pathloss and multipath parameters under LoS and NLoS conditions, respectively. Similarly, the spatially consistent CIR of the uncontrollable channel can be obtained as

$$\begin{aligned}h_p^{\text{env}}(t) = &h_{\text{LoS},p}^{\text{env}}(t) \cdot \text{LoS}_{\text{soft}}^{\text{env}} \\ &+ h_{\text{NLoS},p}^{\text{env}}(t) \cdot \sqrt{1 - (\text{LoS}_{\text{soft}}^{\text{env}})^2} \end{aligned} \tag{31}$$

where $\text{LoS}_{\text{soft}}^{\text{env}}$ is the soft LoS state of uncontrollable channel with the BS-MT LoS probability, i.e., $p_{\text{env}}^{\text{LoS}}(x_{\text{M}}, z_{\text{B}})$. In addition, $h_{\text{LoS},p}^{\text{env}}(t)$ and $h_{\text{NLoS},p}^{\text{env}}(t)$ are the CIR of the uncontrollable channel generated under LoS and NLoS conditions, respectively.

E. Prediction of Optimum UAV Altitude

Lemma 1: Assuming that the RIS controller has the knowledge of the speed and moving direction of the MT, the reflection phases of RIS can be designed to forming a beam to the desired direction $(\vartheta_{\text{des}}^{(1)}, \varphi_{\text{des}}^{(1)})$ as follows

$$\begin{aligned}\psi_n^{\text{opt}}(t) = \text{mod}\Big\{ &-\frac{2\pi}{\lambda}[-v_{\text{M}}t\cos\vartheta_{\text{des}}^{(1)}\cos(\varphi_{\text{des}}^{(1)} - \alpha_{\text{M}}) \\ &+ a_{n_x}(\cos\theta_t^{(1)}\cos\phi_t^{(1)} + \cos\vartheta_{\text{des}}^{(1)}\cos\varphi_{\text{des}}^{(1)}) \\ &+ a_{n_y}(\cos\theta_t^{(1)}\sin\phi_t^{(1)} + \cos\vartheta_{\text{des}}^{(1)}\sin\varphi_{\text{des}}^{(1)})], 2\pi\Big\}. \end{aligned} \tag{32}$$

The proof can be found in [8]. ■

Theorem 1: By applying the optimized reflection phases in (32) and setting $\vartheta_{\text{des}}^{(1)} = \vartheta_r^{(1)}$ and $\varphi_{\text{des}}^{(1)} = \varphi_r^{(1)}$, the average received power of the ARIS-assisted link considering the UAV vibration can be written as $p_r = \bar{p}_r + \tilde{p}_r$ where $\bar{p}_r$ and $\tilde{p}_r$ are average received power of the VLoS and NLoS components, respectively, i.e.,

$$\bar{p}_r = \frac{p_t N^2 \delta_x^2 \delta_y^2 G_t G_r K_1 \cos\varsigma_t \cos\varsigma_r}{16\pi^2(1+K_1)\varepsilon_{\text{BI}}^{n_{\text{PLE}}}\varepsilon_{\text{IM}}^{n_{\text{PLE}}}}\mathbb{E}\{B(A_{n_x}, A_{n_y})^2\} \tag{33}$$

$$\tilde{p}_r = \frac{p_t N \delta_x^2 \delta_y^2 G_t G_r \cos\varsigma_t}{16\pi^2(1+K_1)\varepsilon_{\text{BI}}^{n_{\text{PLE}}}\varepsilon_{\text{IM}}^{n_{\text{PLE}}}}\mathbb{E}\left\{\sum_{l=1}^{L}\sum_{i_l=1}^{I_l}\frac{P_l\cos\varsigma_{r,i_l}}{I_l}\right\} \tag{34}$$

where $\text{sinc}(x) = \frac{\sin(\pi x)}{\pi x}$, p_t is the transmit power, $\mathbb{E}(\cdot)$ is the expectation operation, $B(A_{n_x}, A_{n_y}) = \text{sinc}(\frac{1}{\lambda}N_x\delta_x A_{n_x}) \cdot \text{sinc}(\frac{1}{\lambda}N_y\delta_y A_{n_y})$, A_{n_x}, A_{n_y}, and Φ_n are given in Appendix C.

Proof: See Appendix C. ■

Equation (33) shows that the UAV vibration leads to a reduction in the received power, represented by the power loss term $B(A_{n_x}, A_{n_y})^2$. By setting $\zeta_{\text{Y}}(t)$=$\zeta_{\text{P}}(t)$=$\zeta_{\text{R}}(t)$=0, i.e., removing the effect of UAV vibration, the power loss term reaches the maximum value, i.e., $B(A_{n_x}, A_{n_y})^2 = 1$. Furthermore, the ARIS-assisted channel suffers from severe pathloss, which is proportional to the product of travel distances, i.e.,

$\varepsilon_{\mathrm{BI}} \cdot \varepsilon_{\mathrm{IM}}$. Meanwhile, it reveals that the squared power gain in the order of N^2 still holds, even in the presence of phase mismatch due to UAV vibrations. This suggests that the reduction in received power caused by hardware imperfections and significant pathloss can be mitigated by deploying a larger number of RUs. Considering the soft LoS state, the average received power of the ARIS-assisted link should be updated as [17]

$$p_r = p_{r,\mathrm{LoS}} \cdot (\mathrm{LoS}_{\mathrm{soft}}^{\mathrm{RIS}})^2 + p_{r,\mathrm{NLoS}} \cdot [1 - (\mathrm{LoS}_{\mathrm{soft}}^{\mathrm{RIS}})^2] \tag{35}$$

where $p_{r,\mathrm{LoS}}$ and $p_{r,\mathrm{NLoS}}$ are average received power generated under LoS and NLoS conditions, respectively. Equation (35) reveals that the performance of the ARIS-assisted system critically relies on the UAV altitude. A low altitude of the UAV means a high probability that the VLoS component will be blocked by buildings. When the VLoS component is severely blocked, i.e., $\mathrm{LoS}_{\mathrm{soft}}^{\mathrm{RIS}} = 0$, the signal power is only transmitted by the NLoS component, which suffers from significant multipath fading. Moreover, a low UAV altitude results in large incident and reflection angles of the rays, leading to a small effective aperture of the reflecting elements. However, at a relatively high UAV altitude, the received power is predominantly affected by severe pathloss. We obtain the optimal UAV altitudes by maximizing the average received power in (35) using the stochastic gradient descent (SGD) algorithm.

III. Statistical Properties of the Proposed Channel Model

A. ST-CF

The ST-CF of the model can be defined as [4]

$$\rho_{pp'}(t, \Delta t) = \mathbb{E}\{h_p(t) \cdot h_{p'}^*(t - \Delta t)\} \tag{36}$$

where $(\cdot)^*$ means the complex conjugate operation, Δt represents time difference. Assuming that controllable and uncontrollable channels are independent, by substituting (12) into (36), the ST-CF is further written as [14]

$$\rho_{pp'}(t, \Delta t) = \rho_{pp'}^{\mathrm{RIS}}(t, \Delta t) + \rho_{pp'}^{\mathrm{env}}(t, \Delta t) \tag{37}$$

where

$$\rho_{pp'}^{\mathrm{RIS}}(t, \Delta t) = \bar{\rho}_{pp'}^{\mathrm{RIS}}(t, \Delta t) + \tilde{\rho}_{pp'}^{\mathrm{RIS}}(t, \Delta t) \tag{38}$$

$$\rho_{pp'}^{\mathrm{env}}(t, \Delta t) = \bar{\rho}_{pp'}^{\mathrm{env}}(t, \Delta t) + \tilde{\rho}_{pp'}^{\mathrm{env}}(t, \Delta t). \tag{39}$$

The ST-CF of the VLoS component can be obtained by substituting (19), (32), (70), and (71) into (38) as follows

$$\begin{aligned}\bar{\rho}_{pp'}^{\mathrm{RIS}}(t, \Delta t) = \mathbb{E}\Big\{ & \frac{\delta_x^2 \delta_y^2 K_1 G_t G_r \cos\varsigma_t \cos\varsigma_r}{16\pi^2(1+K_1)\varepsilon_{\mathrm{BI}}^{n_{\mathrm{PLE}}}\varepsilon_{\mathrm{IM}}^{n_{\mathrm{PLE}}}} \\ & \times e^{j\frac{2\pi}{\lambda}\Delta_{\mathrm{B}}[\cos\theta_t^{(1)}\cos\gamma_{\mathrm{B}}^{\mathrm{E}}\cos(\phi_t^{(1)}-\gamma_{\mathrm{B}}^{\mathrm{A}})+\sin\theta_t^{(1)}\sin\gamma_{\mathrm{B}}^{\mathrm{E}}]} \\ & \times \sum_{n=1}^{N}\sum_{n'=1}^{N} e^{j\frac{2\pi}{\lambda}\xi_{\mathrm{Y}}[T_{\mathrm{Y},n,n'}(t,\Delta t)]} \cdot e^{j\frac{2\pi}{\lambda}\xi_{\mathrm{P}}[T_{\mathrm{P},n,n'}(t,\Delta t)]} \\ & \times e^{j\frac{2\pi}{\lambda}\xi_{\mathrm{R}}[T_{\mathrm{R},n,n'}(t,\Delta t)]}\Big\}\end{aligned} \tag{40}$$

with

$$T_{\mathrm{Y},n,n'}(t, \Delta t) = \sin(2\pi f_{\mathrm{Y}} t)\bar{X}_{\mathrm{Y},n} - \sin(2\pi f_{\mathrm{Y}}(t-\Delta t))\bar{X}_{\mathrm{Y},n'} \tag{41}$$

$$T_{\mathrm{P},n,n'}(t, \Delta t) = \sin(2\pi f_{\mathrm{P}} t)\bar{X}_{\mathrm{P},n} - \sin(2\pi f_{\mathrm{P}}(t-\Delta t))\bar{X}_{\mathrm{P},n'} \tag{42}$$

$$T_{\mathrm{R},n,n'}(t, \Delta t) = \sin(2\pi f_{\mathrm{R}} t)\bar{X}_{\mathrm{R},n} - \sin(2\pi f_{\mathrm{R}}(t-\Delta t))\bar{X}_{\mathrm{R},n'} \tag{43}$$

where $\Delta_{\mathrm{B}} = (p'-p)\delta_{\mathrm{B}}$ is the BS antenna spacing between $A_{p'}^t$ and A_p^t. Based on the uniform distributions of vibration angle amplitudes, i.e., $\xi_{\mathrm{Y}} \sim \mathrm{U}(-\zeta_{\mathrm{Y}m}, \zeta_{\mathrm{Y}m})$, $\xi_{\mathrm{P}} \sim \mathrm{U}(-\zeta_{\mathrm{P}m}, \zeta_{\mathrm{P}m})$, and $\xi_{\mathrm{R}} \sim \mathrm{U}(-\zeta_{\mathrm{R}m}, \zeta_{\mathrm{R}m})$ [28], and using the equality $\mathbb{E}\{e^{jtx}\} = \frac{\sin(ta)}{ta}$ for a random variable $x \sim \mathrm{U}(-a, a)$, (40) can be calculated as

$$\begin{aligned}\bar{\rho}_{pp'}^{\mathrm{RIS}}(t, \Delta t) = & \frac{\delta_x^2 \delta_y^2 K_1 G_t G_r \cos\varsigma_t \cos\varsigma_r}{16\pi^2(1+K_1)\varepsilon_{\mathrm{BI}}^{n_{\mathrm{PLE}}}\varepsilon_{\mathrm{IM}}^{n_{\mathrm{PLE}}}} \\ & \times e^{j\frac{2\pi}{\lambda}\Delta_{\mathrm{B}}[\cos\theta_t^{(1)}\cos\gamma_{\mathrm{B}}^{\mathrm{E}}\cos(\phi_t^{(1)}-\gamma_{\mathrm{B}}^{\mathrm{A}})+\sin\theta_t^{(1)}\sin\gamma_{\mathrm{B}}^{\mathrm{E}}]} \\ & \times \sum_{n=1}^{N}\sum_{n'=1}^{N}\int_{-\infty}^{\infty} \mathrm{sinc}\Big(\frac{2}{\lambda}\zeta_{\mathrm{Y}m}\bar{T}_{\mathrm{Y},n,n'}(t,\Delta t)\Big)p(f_{\mathrm{Y}})\mathrm{d}f_{\mathrm{Y}} \\ & \times \int_{-\infty}^{\infty} \mathrm{sinc}\Big(\frac{2}{\lambda}\zeta_{\mathrm{P}m}\bar{T}_{\mathrm{P},n,n'}(t,\Delta t)\Big)p(f_{\mathrm{P}})\mathrm{d}f_{\mathrm{P}} \\ & \times \int_{-\infty}^{\infty} \mathrm{sinc}\Big(\frac{2}{\lambda}\zeta_{\mathrm{R}m}\bar{T}_{\mathrm{R},n,n'}(t,\Delta t)\Big)p(f_{\mathrm{R}})\mathrm{d}f_{\mathrm{R}}\end{aligned} \tag{44}$$

where $p(f_{\mathrm{Y}})$, $p(f_{\mathrm{P}})$, and $p(f_{\mathrm{R}})$ represent the probability density functions (PDFs) of the frequencies of yaw, pitch, and roll angle variations, respectively. Following a similar method, the NLoS component of the ST-CF of the controllable channel can be expressed as

$$\begin{aligned}\tilde{\rho}_{pp'}^{\mathrm{RIS}}(t, \Delta t) = & \frac{\delta_x^2 \delta_y^2 G_t G_r \cos\varsigma_t \cos\varsigma_{r,i_l}}{16\pi^2(1+K_1)\varepsilon_{\mathrm{BI}}^{n_{\mathrm{PLE}}}\varepsilon_{\mathrm{IM}}^{n_{\mathrm{PLE}}}} \\ & \times e^{j\frac{2\pi}{\lambda}\Delta_{\mathrm{B}}[\cos\theta_t^{(1)}\cos\gamma_{\mathrm{B}}^{\mathrm{E}}\cos(\phi_t^{(1)}-\gamma_{\mathrm{B}}^{\mathrm{A}})+\sin\theta_t^{(1)}\sin\gamma_{\mathrm{B}}^{\mathrm{E}}]} \\ & \times \sum_{n=1}^{N}\sum_{n'=1}^{N}\sum_{l=1}^{L}\sum_{i_l=1}^{I_l}\frac{P_l}{I_l}e^{j[\psi_n(t)-\psi_{n'}(t-\Delta t)]}e^{j2\pi\nu_{M,N}\Delta t} \\ & \times \int_{-\infty}^{\infty} \mathrm{sinc}\Big(\frac{2}{\lambda}\zeta_{\mathrm{Y}m}\cdot\tilde{T}_{\mathrm{Y},n,n',i_l}(t,\Delta t)\Big)p(f_{\mathrm{Y}})\mathrm{d}f_{\mathrm{Y}} \\ & \times \int_{-\infty}^{\infty} \mathrm{sinc}\Big(\frac{2}{\lambda}\zeta_{\mathrm{P}m}\cdot\tilde{T}_{\mathrm{P},n,n',i_l}(t,\Delta t)\Big)p(f_{\mathrm{P}})\mathrm{d}f_{\mathrm{P}} \\ & \times \int_{-\infty}^{\infty} \mathrm{sinc}\Big(\frac{2}{\lambda}\zeta_{\mathrm{R}m}\cdot\tilde{T}_{\mathrm{R},n,n',i_l}(t,\Delta t)\Big)p(f_{\mathrm{R}})\mathrm{d}f_{\mathrm{R}}\end{aligned} \tag{45}$$

where

$$\begin{aligned}T_{\mathrm{Y},n,n',i_l}(t, \Delta t) = & \sin(2\pi f_{\mathrm{Y}} t)\tilde{X}_{\mathrm{Y},n,i_l} \\ & - \sin(2\pi f_{\mathrm{Y}}(t-\Delta t))\tilde{X}_{\mathrm{Y},n',i_l}\end{aligned} \tag{46}$$

$$\begin{aligned}T_{\mathrm{P},n,n',i_l}(t, \Delta t) = & \sin(2\pi f_{\mathrm{P}} t)\tilde{X}_{\mathrm{P},n,i_l} \\ & - \sin(2\pi f_{\mathrm{P}}(t-\Delta t))\tilde{X}_{\mathrm{P},n',i_l}\end{aligned} \tag{47}$$

$$\begin{aligned}T_{\mathrm{R},n,n',i_l}(t, \Delta t) = & \sin(2\pi f_{\mathrm{R}} t)\tilde{X}_{\mathrm{R},n,i_l} \\ & - \sin(2\pi f_{\mathrm{R}}(t-\Delta t))\tilde{X}_{\mathrm{R},n',i_l}.\end{aligned} \tag{48}$$

Based on (26) and (27), the LoS and NLoS components of the uncontrollable channel can be respectively expressed as

$$\bar{\rho}^{\text{env}}_{pp'}(t,\Delta t) = \frac{K_2 \text{PL}^{-1}_{\text{env}}}{K_2+1} e^{j\frac{2\pi}{\lambda}\Delta t[-v_{\text{M}}\cos\vartheta^{(2)}_r \cos(\varphi^{(2)}_r-\alpha_{\text{M}})]} \times e^{j\frac{2\pi}{\lambda}\Delta_{\text{B}}[\sin\theta^{(2)}_t \sin\gamma^{\text{E}}_{\text{B}}+\cos\theta^{(2)}_t\cos\gamma^{\text{E}}_{\text{B}}\cos(\phi^{(2)}_t-\gamma^{\text{A}}_{\text{B}})]} \quad (49)$$

$$\tilde{\rho}^{\text{env}}_{pp'}(t,\Delta t) = \frac{\text{PL}^{-1}_{\text{env}}}{K_2+1}\sum_{s=1}^{S}\sum_{i_s=1}^{I_s}\frac{P_s}{I_s} \times e^{j\frac{2\pi}{\lambda}\Delta_{\text{B}}[\cos\theta_{i_s}\cos\gamma^{\text{E}}_{\text{B}}\cos(\phi_{i_s}-\gamma^{\text{A}}_{\text{B}})+\sin\theta_{i_s}\sin\gamma^{\text{E}}_{\text{B}}]} \times e^{j\frac{2\pi}{\lambda}\Delta_t[-v_{\text{M}}\cos\vartheta_{i_s}\cos(\varphi_{i_s}-\alpha_{\text{M}})]}. \quad (50)$$

The spatially consistent ST-CF of the controllable and uncontrollable channels with soft LoS states can be obtained by updating (38) and (39) as follows

$$\rho^{\text{RIS}}_{pp'}(t,\Delta t) = \rho^{\text{RIS}}_{\text{LoS},pp'}(t,\Delta t)\cdot(\text{LoS}^{\text{RIS}}_{\text{soft}})^2 + \rho^{\text{RIS}}_{\text{NLoS},pp'}(t,\Delta t)\cdot[1-(\text{LoS}^{\text{RIS}}_{\text{soft}})^2] \quad (51)$$

$$\rho^{\text{env}}_{pp'}(t,\Delta t) = \rho^{\text{env}}_{\text{LoS}}(t,\Delta t)\cdot(\text{LoS}^{\text{env}}_{\text{soft}})^2 + \rho^{\text{env}}_{\text{NLoS},pp'}(t,\Delta t)\cdot[1-(\text{LoS}^{\text{env}}_{\text{soft}})^2] \quad (52)$$

where $\rho^{\text{RIS}}_{\text{LoS},pp'}(t,\Delta t)$ and $\rho^{\text{RIS}}_{\text{NLoS},pp'}(t,\Delta t)$ are the ST-CF of the controllable channel generated under LoS and NLoS conditions, respectively. Similarly, $\rho^{\text{env}}_{\text{LoS},pp'}(t,\Delta t)$ and $\rho^{\text{env}}_{\text{NLoS},pp'}(t,\Delta t)$ are the ST-CF of the uncontrollable channel generated under LoS and NLoS conditions, respectively.

B. Doppler PSD

The Doppler PSD provides insights into the frequency spreading of time-varying nature of the channel, and can be obtained as $S(\nu) = \int_{-\infty}^{\infty}\rho_{pp'}(t,\Delta t)e^{-j2\pi\nu\Delta t}\text{d}\Delta t$. The Doppler PSD of the proposed model is further expressed as

$$S(\nu) = (\text{LoS}^{\text{RIS}}_{\text{soft}})^2 S^{\text{RIS}}_{\text{LoS}}(\nu) + (\text{LoS}^{\text{env}}_{\text{soft}})^2 S^{\text{env}}_{\text{LoS}}(\nu) + [1-(\text{LoS}^{\text{RIS}}_{\text{soft}})^2]S^{\text{RIS}}_{\text{NLoS}}(\nu) + [1-(\text{LoS}^{\text{env}}_{\text{soft}})^2]S^{\text{env}}_{\text{NLoS}}(\nu) \quad (53)$$

where

$$S^{\text{RIS}}_{\text{LoS}}(\nu) = \int_{-\infty}^{\infty}\rho^{\text{RIS}}_{\text{LoS},pp'}(t,\Delta t)e^{-j2\pi\nu\Delta t}\text{d}\Delta t \quad (54)$$

$$S^{\text{env}}_{\text{LoS}}(\nu) = \int_{-\infty}^{\infty}\rho^{\text{env}}_{\text{LoS},pp'}(t,\Delta t)e^{-j2\pi\nu\Delta t}\text{d}\Delta t \quad (55)$$

$$S^{\text{RIS}}_{\text{NLoS}}(\nu) = \int_{-\infty}^{\infty}\rho^{\text{RIS}}_{\text{NLoS},pp'}(t,\Delta t)e^{-j2\pi\nu\Delta t}\text{d}\Delta t \quad (56)$$

$$S^{\text{env}}_{\text{NLoS}}(\nu) = \int_{-\infty}^{\infty}\rho^{\text{env}}_{\text{NLoS},pp'}(t,\Delta t)e^{-j2\pi\nu\Delta t}\text{d}\Delta t. \quad (57)$$

IV. Results and Analysis

In this section, the statistics of the proposed model are presented and discussed. Unless otherwise specified, the model parameters are selected as follows: $f_c = 28$ GHz, $P = 4$, $K_1 = K_2 = 5$ dB, $G_t = G_r = 1$ [32], $z_{\text{B}} = 10$ m, $x_{\text{M}} = 400$ m, $(x_{\text{U}}, y_{\text{U}}, z_{\text{U}}) = (60\text{ m}, 20\text{ m}, 100\text{ m})$, $N_x = N_y = 100$, $\delta_x = \delta_y = \lambda/5$, $\delta_{\text{B}} = \lambda/2$, $v_{\text{M}} = 3$ m/s, $\alpha_{\text{M}} = \pi/6$, $\gamma^{\text{A}}_{\text{B}} = \pi/4$, $\gamma^{\text{E}}_{\text{B}} = \pi/6$, $\zeta_{\text{X}m} = 1°$, $f_{\text{X}} \sim \text{U}(5,25)$, $\text{X} \in \{\text{Y, P, R}\}$, and $p_t = 20$ dBm. The environment-related parameters are collected in Table II [29], [33], [34]. Besides, the parameters such as powers and angles of multipath components in different scenarios are randomly generated according to the standard 5G channel model [5], [17].

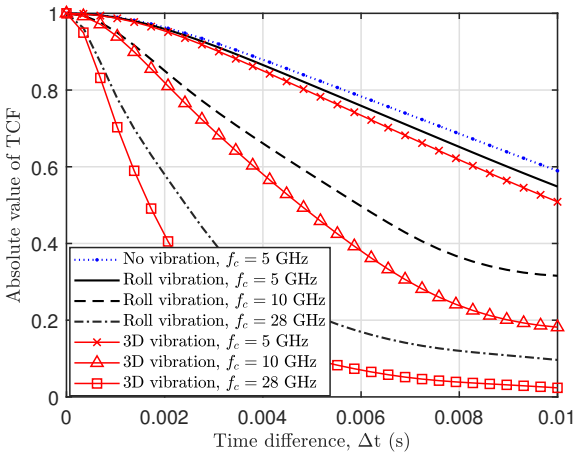

Fig. 3. The TCFs of the proposed model with different degrees of UAV vibrations and carrier frequencies ($\alpha_0 = 0.1$, $\beta_0 = 750/\text{km}^2$, $\gamma_0 = 8$ m).

TABLE II
Environmental Parameters.

Parameters	Value
Scenario	Suburban, Urban, Dense urban
Building area ratio (α_0)	0.1, 0.3, 0.5
Number of buildings (β_0)	750/km^2, 500/km^2, 300/km^2
Average building height (γ_0)	8 m, 15 m, 20 m
PLE in LoS condition	2.0, 2.0, 2.1
PLE in NLoS condition	2.5, 3.0, 3.4

Fig. 3 compares the temporal CFs (TCFs) of the proposed model under varying degrees of UAV vibration and carrier frequencies. The channel exhibits the highest temporal correlation by eliminating the effects of UAV vibration. In this case, the adjustable reflecting phases effectively mitigate multipath and Doppler effects caused by MT movement. Compared to TCFs with one-dimensional UAV vibration, the TCFs with 3D vibration are lower, indicating faster time variations of the channel and resulting in a shorter channel coherence time. For a given level of UAV vibration, the channel becomes more susceptible to vibration effects when the system operates in higher frequency bands. This observation aligns with the derivation in (20), indicating that higher carrier frequencies (or shorter wavelengths) result in larger Doppler frequencies due to UAV vibration, leading to significant phase misalignment of signals reflected by the RIS.

Fig. 4 illustrates the TCF of the proposed model under different vibration angles and ARIS configurations. Under the same RIS configuration, the UAV wobbling in different dimensions has distinct impacts on TCFs. The channel exhibits the highest temporal correlation when the ARIS oscillates parallel to the xy plane. Roll vibrations result in lower temporal correlation compared to pitch vibrations. Furthermore, we find that the impact of UAV vibrations is strongly influenced by the RIS configurations. The channel with 50×100 RIS (i.e., $N_x = 50, N_y = 100$) is more susceptible to yaw vibrations

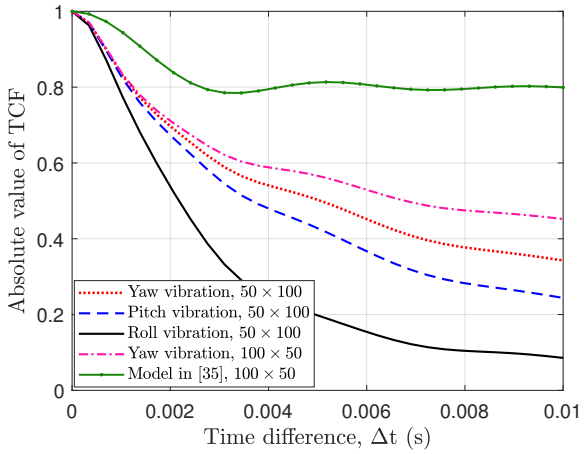

Fig. 4. The TCFs of the proposed model with different UAV vibration angles and ARIS configurations ($\alpha_0 = 0.1$, $\beta_0 = 750/\text{km}^2$, $\gamma_0 = 8$ m).

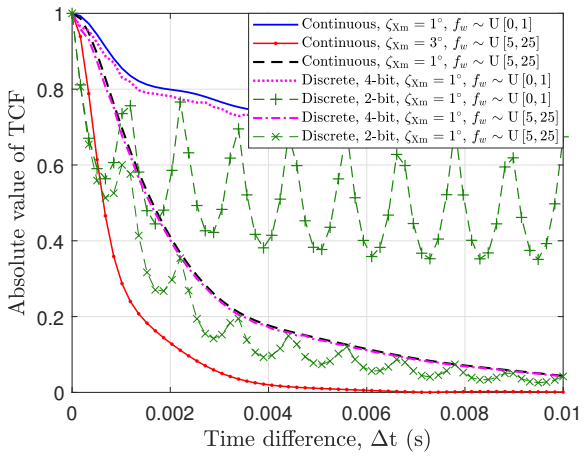

Fig. 5. The TCFs of propose model with different amplitudes and variation frequencies of the vibration angles ($\alpha_0 = 0.1$, $\beta_0 = 750/\text{km}^2$, $\gamma_0 = 8$ m, X $\in$ {Y, P, R}).

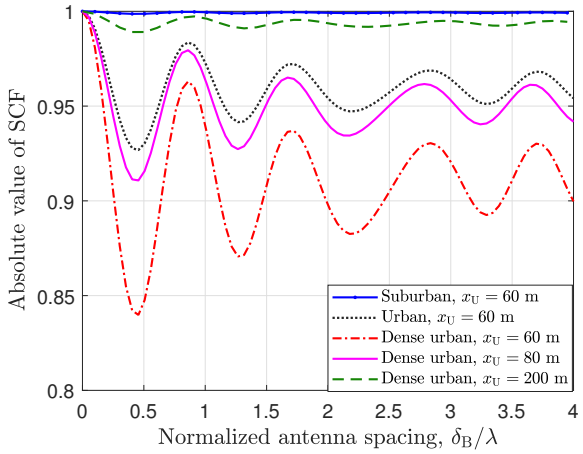

Fig. 6. The SCFs of the proposed channel model under various scenarios and UAV locations.

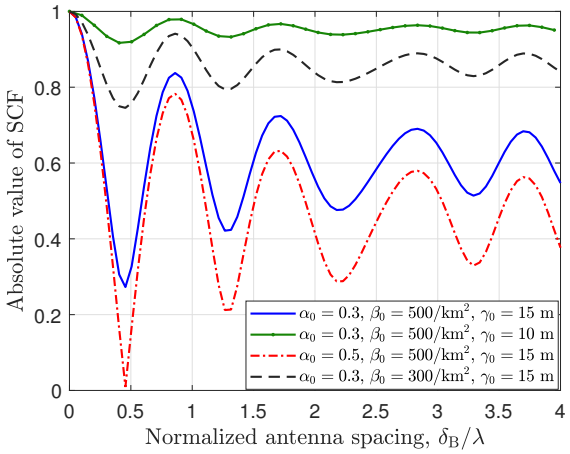

Fig. 7. SCFs of the proposed channel model using different environmental parameters.

compared to the channel with 100×50 RIS. This is because, for a 50×100 RIS, yaw vibrations cause more significant variations in the travel distance of the waves, as the waves propagate mainly along the x axis. The study in [35] assumes constant vibration angles instead of modeling them as random processes and neglects the blocking probability of the VLoS component, leading to a higher temporal correlation compared to the proposed model.

Fig. 5 illustrates the TCFs of the proposed model with varying amplitudes and frequencies of vibration angles. The temporal correlation decreases as the amplitude or frequency of the vibration angles increases. Additionally, the channel exhibits similar performance in TCFs when using continuous and 4-bit discrete reflection phases. However, a significant decrease in TCF is observed when using 2-bit discrete reflection phases, attributed to the increased quantization errors. This indicates that a higher number of quantization levels is necessary to minimize the time variation of the channel, particularly under adverse weather conditions.

Fig. 6 shows the spatial CF (SCF) of the proposed model in suburban, urban, and dense urban scenarios with different UAV locations. The channel exhibits the highest spatial correlation in the suburban scenario. This is attributed to the relatively open propagation environment, where the channel is dominated by a strong VLoS component, significantly mitigating multipath fading. Conversely, in dense urban scenarios, the SCF decreases more rapidly due to the small LoS probability and high PLEs. Additionally, within the same scenario, a shorter distance between the UAV and MT results in a higher LoS probability in the RIS-MT channel, which means the beam directed towards the MT is less likely to be obstructed, thereby increasing the spatial correlation of the channel.

To better illustrate the impact of environmental factors, Fig. 7 displays the SCFs of the proposed model under different environmental parameters. For a meaningful comparison, we use the urban scenario as a benchmark, i.e., $\alpha_0 = 0.3$, $\beta_0 = 500$ km^2, and $\gamma_0 = 15$ m. The results indicate that a higher built-up land ratio (α_0) or building density (β_0) leads to an increase in the average number of buildings along the

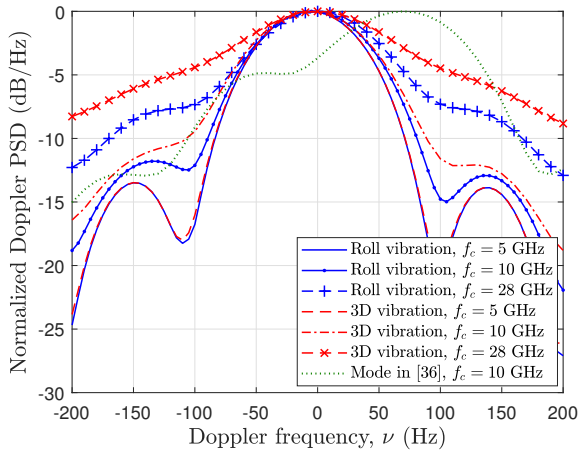

Fig. 8. Impacts of UAV vibrations and carrier frequencies on Doppler PSDs of the proposed model ($\alpha_0 = 0.1$, $\beta_0 = 750/\text{km}^2$, $\gamma_0 = 8$ m).

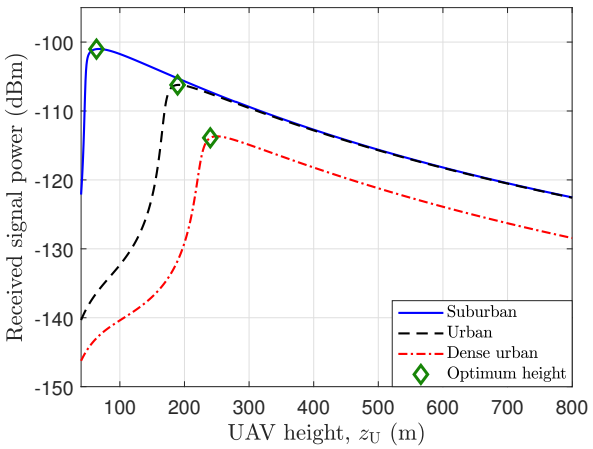

Fig. 9. Variation of average received signal power with respect to the UAV height for different scenarios.

LoS path. This in turn raises the blockage probability of the VLoS component and decreases the spatial correlation of the channel. Besides, lower values of average building height (γ_0) can significantly increase the VLoS probability and thereby enhance the spatial correlation of the channel.

Fig. 8 shows the impacts of UAV vibrations and carrier frequencies on the Doppler PSDs of the proposed model. At low-frequency bands, i.e., 5 GHz, the effect of UAV vibration can be negligible. With the increase of carrier frequency, the Doppler PSD tends to spread widely over the Doppler frequencies. For given frequency bands, i.e., 10 GHz and 28 GHz, 3D vibration results in a wider range of the spectrum compared to one-dimensional yaw vibration. We compare the Doppler PSD of the proposed model to that generated by the model in [36]. Although the reflection phases in [36] can effectively eliminate multipath fading, they cannot offset the phase shift induced by the Doppler frequencies.

Fig. 9 shows the variation in average received signal power with respect to the UAV height for different scenarios. The optimal UAV height is determined by maximizing (35) using

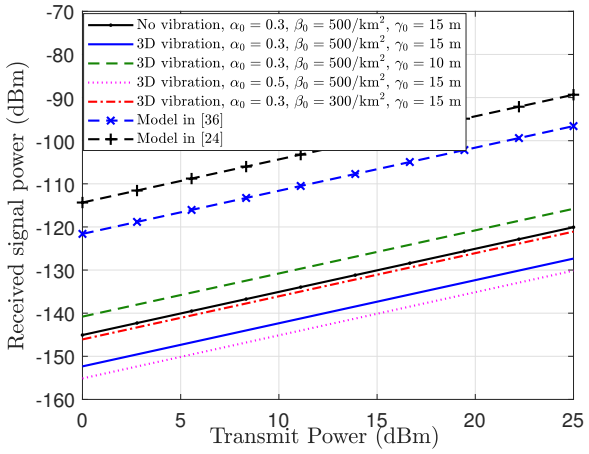

Fig. 10. The effects of UAV vibration and environmental parameters on the average received signal power.

the SGD algorithm. In the suburban scenario, buildings are relatively low and sparse. As the UAV height increases, the LoS probability in the RIS-MT link rapidly increases, leading to a swift rise in received signal power. However, as the UAV continue to ascend, the received signal power decreases due to increased pathloss. Among the three scenarios, the suburban scenario has the lowest optimal UAV height. Conversely, the dense urban scenario requires the highest optimal UAV altitude to establish a robust LoS path to the MT, owing to the dense and tall building distribution. As the UAV altitude increases, the LoS probability of the RIS-MT link approaches one, and the channel is mainly dominated by the strong LoS component. As a result, the received powers in suburban and urban scenarios converge to the same value due to the identical PLE, i.e., $n_{\text{PLE}} = 2$. However, in the dense urban scenario, the received power is lower due to a higher PLE, i.e., $n_{\text{PLE}} = 2.1$.

Fig. 10 illustrates the effects of UAV vibration and environmental parameters on the average received signal power. Under the same environmental conditions, UAV vibration reduces received power due to the misalignment of reflected signal phases. Additionally, a higher built-up land ratio or building density indicates a denser propagation environment, increasing the probability of VLoS component blockage and decreasing average received power. Conversely, lower average building height tends to increase the average received power. The results of the proposed model are compared with those generated by [24] and [36] using the same model parameters. Note that the model in [24] neglects UAV wobbling. The model in [36] considers only pitch and roll wobbles, which are modeled by uniform distributions. Although the yaw wobble does not change the effective apertures of RUs, it causes fluctuations in the transmission distances between RUs and ground nodes. This results in phase misalignment of the reflected signals, which leads to reduced received signal power, as shown in (33). Furthermore, the models in [24] and [36] assume robust LoS connections between the UAV and ground nodes, even at low UAV altitudes. This assumption may be inconsistent with realistic propagation environments and leads

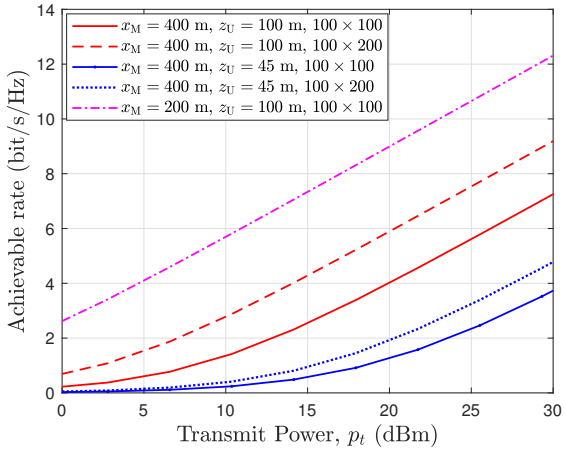

Fig. 11. Achievable rates of the ARIS system under varying RIS configurations and different UAV and RIS positions ($\alpha_0 = 0.1$, $\beta_0 = 750/\text{km}^2$, $\gamma_0 = 8$ m).

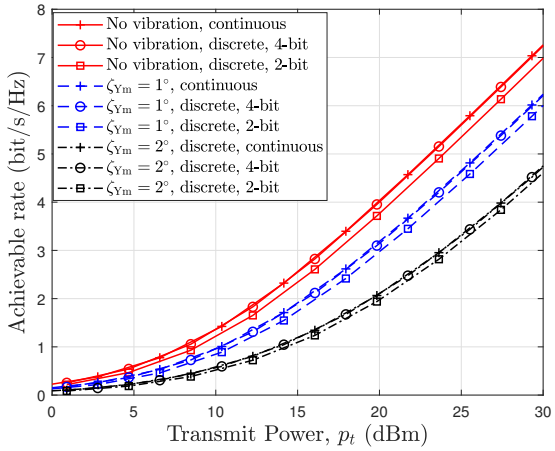

Fig. 12. Achievable rates of the ARIS system with continuous and discrete reflection phases ($\alpha_0 = 0.1$, $\beta_0 = 750/\text{km}^2$, $\gamma_0 = 8$ m).

to an overestimation of the system performance.

Fig. 11 shows the achievable rates of the ARIS system under varying RIS configurations and different UAV and RIS positions. By adopting the maximum ratio transmitting, the achievable rates are calculated as $R = \mathbb{E}\left\{\log_2\left(1 + \frac{p_t}{\sigma^2}\|\mathbf{h}\|^2\right)\right\}$, where the noise power is $\sigma^2 = -100$ dBm [37]. For the cases of $x_M = 400$ m and $z_U = 100$ m, a significant improvement can be achieved with the use of a larger RIS. However, a significant degradation occurs when the UAV altitude is reduced to 45 meters, and only a minor improvement is observed with a larger RIS when the UAV hovers at lower altitudes. This is because a lower UAV altitude reduces the LoS probability of the RIS-MT link and leads to a smaller effective aperture of RUs, thereby decreasing the benefits of the ARIS. Furthermore, a smaller value of x_M increases the LoS probabilities of the Tx-MT and RIS-MT subchannels and simultaneously decreasing the corresponding pathlosses, resulting in a remarkable increase in the achievable rate.

Fig. 12 shows the achievable rates of the ARIS system with discrete and continuous phases. For b-bit phase resolution, the discrete phases are obtained by quantizing the continuous phases to the nearest point in $\{0, \frac{2\pi}{2^b}, \ldots, \frac{2\pi}{2^b}(2^b - 1)\}$. With the increase of the amplitude of vibration angle, significant degradation in achievable rates is observed. Additionally, it is shown that the channel behaves similarly in terms of achievable rates when using continuous and 4-bit reflection phases. As the quantization level reduces to 2-bit, quantization error becomes noticeable. Furthermore, we find that at larger degrees of vibration, ARIS system becomes less sensitive to the quantization level. This is because the phase misalignment reduces the constructive effect of the controllable channel, and the proportion of the received power from the VLoS component in the total received power decreases.

V. Conclusions

A novel channel model for ARIS-assisted communications has been presented in this paper. UAV vibrations in 3D space due to adverse weather conditions have been characterized by yaw, pitch, and roll angles, and modeled as sinusoidal random processes. The effects of UAV vibrations have been represented through the derivation of approximate expressions that calculate the time variation in the travel distances of reflected waves. We have demonstrated that UAV vibrations cause phase misalignment in reflected signals and induce additional Doppler shifts. The final CIR has been obtained based on soft LoS states, determined by environmental parameters such as built-up land ratio, building density, and average building height. The optimal UAV altitude has been derived by balancing LoS probability, pathloss, and the effective apertures of RUs. Channel characteristics, including ST-CF, Doppler PSD, average received signal power, and the achievable rate of the model, have been analyzed. The results indicate that a large degree of UAV vibration, whether in the frequency or amplitude of vibration angles, can significantly reduce temporal correlation and increase the Doppler spread of the channel, which are more pronounced at higher frequency bands. Moreover, dense or tall-building environments, as well as adverse weather conditions, can reduce the average received signal power and degrade the achievable rate of the ARIS system. However, these can be mitigated by employing a large number of RUs and carefully optimizing the UAV altitude. Furthermore, compared to continuous reflection phases, 2-bit and 4-bit discrete phases do not cause significant degradation in achievable rates, even in environments with substantial UAV vibration, confirming the practicality of ARIS systems.

Appendix A

Derivation of (14)

The CIR of the VLoS component can be obtained by summing the rays reflected by the N RUs, i.e., [38]

$$\bar{h}_p^{\text{RIS}}(t) = \sqrt{\frac{K_1\beta_t\beta_r}{K_1+1}} \sum_{n=1}^{N} e^{j\psi_n(t)} \cdot e^{j\chi_{pn}(t)} \cdot e^{j\chi_{\text{MT},n}(t)} \quad (58)$$

where β_t and β_r are channel gains of the BS-RIS and RIS-MT links, respectively, i.e.,

$$\beta_t = \mathrm{PL}_t^{-1} G_t G_e(\mathbf{r}_{\text{in}}) \tag{59}$$

$$\beta_r = \mathrm{PL}_r^{-1} G_r G_e(\mathbf{r}_{\text{out}}) \tag{60}$$

where $G_e(\mathbf{r}_{\text{in}})$ and $G_e(\mathbf{r}_{\text{out}})$ account for the gains of the RU in the directions of $\mathbf{r}_{\text{in}}$ and $\mathbf{r}_{\text{out}}$, respectively. For a wave impinges on the RIS, the effective aperture of a RU is defined as [39]

$$A_e(\mathbf{r}_{\text{in}}) = G_e(\mathbf{r}_{\text{in}}) \cdot A_{\text{iso}} \tag{61}$$

where $A_{\text{iso}} = \frac{\lambda^2}{4\pi}$ is the effective aperture of an lossless isotropic antenna. Considering a RU with the physical area $\delta_x \delta_y$, its effective aperture is calculated as $\delta_x \delta_y \cos\varsigma_t$, where ς_t is the angle between the impinging waves and the normal direction of the RIS. Thus, we have

$$G_e(\mathbf{r}_{\text{in}}) = \frac{4\pi}{\lambda^2} \delta_x \delta_y \cos\varsigma_t. \tag{62}$$

Similarly, $G_e(\mathbf{r}_{\text{out}})$ is obtained as

$$G_e(\mathbf{r}_{\text{out}}) = \frac{4\pi}{\lambda^2} \delta_x \delta_y \cos\varsigma_r. \tag{63}$$

Substituting (59), (60), (62), and (63) into (58), we obtain (14).

APPENDIX B

Derivation of (16)

The distance from the BS array center to the U_n at time t is calculated as

$$\varepsilon_{\text{BS},n}(t) = \left\| \mathbf{d}_{\text{BI}} + \mathbf{d}_n^{\text{wob}}(t) \right\| \tag{64}$$

where

$$\mathbf{d}_{\text{BI}} = \varepsilon_{\text{BI}} \cdot \left[\cos\theta_t^{(1)} \cos\phi_t^{(1)}, \cos\theta_t^{(1)} \sin\phi_t^{(1)}, \sin\theta_t^{(1)} \right]^{\mathrm{T}}. \tag{65}$$

By subsituting the (11) and (65) into (64), we have

$$\begin{aligned}
\varepsilon_{\text{BS},n}(t) = \{ & [\cos\zeta_{\mathrm{Y}}(t) \cdot \cos\zeta_{\mathrm{P}}(t) \cdot a_{n_x} \\
& + (\cos\zeta_{\mathrm{Y}}(t) \cdot \sin\zeta_{\mathrm{R}}(t) \cdot \sin\zeta_{\mathrm{P}}(t) - \sin\zeta_{\mathrm{Y}}(t) \\
& \times \cos\zeta_{\mathrm{R}}(t)) a_{n_y} + \varepsilon_{\text{BI}} \cdot \cos\theta_t^{(1)} \cdot \cos\phi_t^{(1)}]^2 + [\sin\zeta_{\mathrm{Y}}(t) \\
& \times \cos\zeta_{\mathrm{P}}(t) a_{n_x} + (\sin\zeta_{\mathrm{Y}}(t) \cdot \sin\zeta_{\mathrm{R}}(t) \cdot \sin\zeta_{\mathrm{P}}(t) + \cos\zeta_{\mathrm{Y}}(t) \\
& \times \cos\zeta_{\mathrm{R}}(t)) \cdot a_{n_y} + \varepsilon_{\text{BI}} \cdot \cos\theta_t^{(1)} \cdot \sin\phi_t^{(1)}]^2 + [-\sin\zeta_{\mathrm{P}}(t) \\
& \times a_{n_x} + \cos\zeta_{\mathrm{P}}(t) \cdot \sin\zeta_{\mathrm{R}}(t) a_{n_y} + \varepsilon_{\text{BI}} \cdot \sin\theta_t^{(1)}]^2 \}^{1/2}.
\end{aligned} \tag{66}$$

Assuming the far-field condition, i.e., $\{a_{n_x}, a_{n_y}\} \ll \varepsilon_{\text{BI}}$, and using the approximation $\sqrt{1-x} \approx 1 - \frac{x}{2}$ when x is small, (66) is approximated as

$$\begin{aligned}
\varepsilon_{\text{BS},n}(t) \approx \varepsilon_{\text{BI}} + \{ & [\cos\zeta_{\mathrm{Y}}(t) \cdot \cos\zeta_{\mathrm{P}}(t) \cdot a_{n_x} \\
& + (\cos\zeta_{\mathrm{Y}}(t) \cdot \sin\zeta_{\mathrm{R}}(t) \cdot \sin\zeta_{\mathrm{P}}(t) - \sin\zeta_{\mathrm{Y}}(t) \\
& \times \cos\zeta_{\mathrm{R}}(t)) a_{n_y}] \cdot \cos\theta_t^{(1)} \cdot \cos\phi_t^{(1)} + [\sin\zeta_{\mathrm{Y}}(t) \\
& \times \cos\zeta_{\mathrm{P}}(t) a_{n_x} + (\sin\zeta_{\mathrm{Y}}(t) \cdot \sin\zeta_{\mathrm{R}}(t) \cdot \sin\zeta_{\mathrm{P}}(t) \\
& + \cos\zeta_{\mathrm{Y}}(t) \cos\zeta_{\mathrm{R}}(t)) \cdot a_{n_y}] \cdot \cos\theta_t^{(1)} \cdot \cos\phi_t^{(1)} \\
& + [-\sin\zeta_{\mathrm{P}}(t) a_{n_x} + \cos\zeta_{\mathrm{P}}(t) \cdot \sin\zeta_{\mathrm{R}}(t) \cdot a_{n_y}] \cdot \sin\theta_t^{(1)} \}.
\end{aligned} \tag{67}$$

Noting that $\max\{\zeta_{\mathrm{Y}}(t), \zeta_{\mathrm{P}}(t), \zeta_{\mathrm{R}}(t)\} \ll 1$, by applying the approximations $\sin(\zeta_x(t)) \approx \zeta_x(t)$ and $\cos(\zeta_x) \approx 1$ to (67), where $x \in \{\mathrm{Y}, \mathrm{P}, \mathrm{R}\}$, we can obtain (16).

APPENDIX C

Derivation of (33) *and* (34)

The average received signal power of the BS-ARIS-MT link can be defined as [40]

$$p_r = \mathbb{E}[\frac{p_t}{P} \left\| \bar{\mathbf{h}}_{\text{RIS}} + \tilde{\mathbf{h}}_{\text{RIS}} \right\|^2] \tag{68}$$

where $\bar{\mathbf{h}}_{\text{RIS}} = [\bar{h}_p^{\text{RIS}}(t)]_{1\times P}$, $\tilde{\mathbf{h}}_{\text{RIS}} = [\tilde{h}_p^{\text{RIS}}(t)]_{1\times P}$. Note that $\bar{\mathbf{h}}_{\text{RIS}}$ and $\tilde{\mathbf{h}}_{\text{RIS}}$ are independent with each other and $\mathbb{E}\{\tilde{h}_p^{\text{RIS}}(t)\} = 0$ [14], using $\|\mathbf{A}\|^2 = \mathrm{tr}(\mathbf{A}^{\mathrm{H}}\mathbf{A})$, we have

$$\begin{aligned}
p_r &= \bar{p}_r + \tilde{p}_r \\
&= \frac{p_t}{P} \mathrm{tr}\{\mathbb{E}(\bar{\mathbf{H}}_{\text{RIS}}^{\mathrm{H}} \bar{\mathbf{H}}_{\text{RIS}})\} + \frac{p_t}{P} \mathrm{tr}\{\mathbb{E}(\tilde{\mathbf{H}}_{\text{RIS}}^{\mathrm{H}} \tilde{\mathbf{H}}_{\text{RIS}})\}.
\end{aligned} \tag{69}$$

For the VLoS component, the pahtlosses of BS-ARIS and ARIS-MT are converted into linear scale as

$$\mathrm{PL}_t = (\frac{4\pi}{\lambda})^2 \varepsilon_{\text{BI}}^{n_{\text{PLE}}} \tag{70}$$

$$\mathrm{PL}_r = (\frac{4\pi}{\lambda})^2 \varepsilon_{\text{IM}}^{n_{\text{PLE}}}. \tag{71}$$

By substituting (70), (71), and (32) into (19), we have

$$\begin{aligned}
\bar{h}_p^{\text{RIS}}(t) = & \frac{\delta_x \delta_y}{4\pi} \sqrt{\frac{K_1 G_t G_r \cos\varsigma_t \cos\varsigma_r}{(1+K_1) \varepsilon_{\text{BI}}^{n_{\text{PLE}}} \varepsilon_{\text{IM}}^{n_{\text{PLE}}}}} \\
& \times e^{j\frac{2\pi}{\lambda}\Delta_p[\cos\theta_t^{(1)} \cos\gamma_{\mathrm{B}}^{\mathrm{E}} \cos(\phi_t^{(1)} - \gamma_{\mathrm{B}}^{\mathrm{A}}) + \sin\theta_t^{(1)} \sin\gamma_{\mathrm{B}}^{\mathrm{E}}]} \\
& \times e^{j\frac{2\pi}{\lambda}(\varepsilon_{\text{IM}} + \varepsilon_{\text{BI}})} \cdot e^{j\frac{2\pi}{\lambda}(\frac{N_x+1}{2}\delta_x A_{n_x} + \frac{N_y+1}{2}\delta_x A_{n_x})} \\
& \times \sum_{n_x=1}^{N_x} \sum_{n_y=1}^{N_y} e^{-j\frac{2\pi}{\lambda} n_x \delta_x A_{n_x}} e^{-j\frac{2\pi}{\lambda} n_y \delta_y A_{n_y}}
\end{aligned} \tag{72}$$

where

$$\begin{aligned}
A_{n_x} = & \zeta_{\mathrm{Y}}(t)(\cos\theta_t^{(1)} \sin\phi_t^{(1)} + \cos\vartheta_r^{(1)} \sin\varphi_r^{(1)}) \\
& + \zeta_{\mathrm{P}}(t)(-\sin\theta_t^{(1)} - \sin\vartheta_r^{(1)})
\end{aligned} \tag{73}$$

$$\begin{aligned}
A_{n_y} = & \zeta_{\mathrm{Y}}(t)(-\cos\theta_t^{(1)} \cos\phi_t^{(1)} - \cos\vartheta_r^{(1)} \cos\varphi_r^{(1)}) \\
& + \zeta_{\mathrm{R}}(t)(\sin\theta_t^{(1)} + \sin\vartheta_r^{(1)}).
\end{aligned} \tag{74}$$

Note the $\zeta_{\mathrm{Y}}(t)$, $\zeta_{\mathrm{P}}(t)$, and $\zeta_{\mathrm{R}}(t)$ are small angles, following the summation formula for geometric series and applying $\sin(x) \approx x$, (72) can be solved as

$$\begin{aligned}
\bar{h}_p^{\text{RIS}}(t) = & \frac{N_x N_y \delta_x \delta_y}{4\pi} \sqrt{\frac{K_1 G_t G_r \cos\varsigma_t \cos\varsigma_r}{(1+K_1) \varepsilon_{\text{BI}}^{n_{\text{PLE}}} \varepsilon_{\text{IM}}^{n_{\text{PLE}}}}} \\
& \times e^{j\frac{2\pi}{\lambda}\Delta_p[\cos\theta_t^{(1)} \cos\gamma_{\mathrm{B}}^{\mathrm{E}} \cos(\phi_t^{(1)} - \gamma_{\mathrm{B}}^{\mathrm{A}}) + \sin\theta_t^{(1)} \sin\gamma_{\mathrm{B}}^{\mathrm{E}}]} \\
& \times e^{j\frac{2\pi}{\lambda}(\varepsilon_{\text{IM}} + \varepsilon_{\text{BI}})} \cdot \mathrm{sinc}(\frac{1}{\lambda} N_x \delta_x A_{n_x}) \cdot \mathrm{sinc}(\frac{1}{\lambda} N_y \delta_y A_{n_y}).
\end{aligned} \tag{75}$$

By substituting (75) into (69), the average received power of the VLoS component can be obtained as

$$\begin{aligned}
\bar{p}_r = & \frac{p_t N^2 \delta_x^2 \delta_y^2 G_t G_r K_1 \cos\varsigma_t \cos\varsigma_r}{16\pi^2 (1+K_1) \varepsilon_{\text{BI}}^{n_{\text{PLE}}} \varepsilon_{\text{IM}}^{n_{\text{PLE}}}} \\
& \times \mathbb{E}\Big\{ \mathrm{sinc}^2(\frac{1}{\lambda} N_x \delta_x A_{n_x}) \cdot \mathrm{sinc}^2(\frac{1}{\lambda} N_y \delta_y A_{n_y}) \Big\}.
\end{aligned} \tag{76}$$

The average received power of the NLoS component can be calculated based on the uncorrelated scattering assumption and following a similar procedure.

REFERENCES

[1] J. Huang, C.-X. Wang, Y. Sun, R. Feng, J. Huang, B. Guo, Z. Zhong, and T. J. Cui, "Reconfigurable intelligent surfaces: Channel characterization and modeling," *Proc. IEEE*, vol. 110, no. 9, pp. 1290–1311, Sept. 2022.

[2] Q. Wu, S. Zhang, B. Zheng, C. You, and R. Zhang, "Intelligent reflecting surface-aided wireless communications: A tutorial," *IEEE Trans. Commun.*, vol. 69, no. 5, pp. 3313–3351, Jan. 2021.

[3] C.-X. Wang *et al.*, "On the road to 6G: Visions, requirements, key technologies, and testbeds," *IEEE Commun. Surveys Tuts.*, vol. 25, no. 2, pp. 905–974, 2023.

[4] J. Bian, C.-X. Wang, X. Gao, X. You, and M. Zhang, "A general 3D non-stationary wireless channel model for 5G and beyond," *IEEE Trans. Wireless Commun.*, vol. 20, no. 5, pp. 3211–3224, Jan. 2021.

[5] C.-X. Wang, Z. Lv, X. Gao, X. You, Y. Hao, and H. Haas, "Pervasive wireless channel modeling theory and applications to 6G GBSMs for all frequency bands and all scenarios," *IEEE Trans. Veh. Technol.*, vol. 71, no. 9, pp. 9159–9173, Sept. 2022.

[6] S. W. Ellingson, "Path loss in reconfigurable intelligent surface-enabled channels," in *Proc. PIMRC'21*, Helsinki, Finland, Oct. 2021, pp. 829–835.

[7] F. Y. A.Z. Elsherbeni and P. Nayeri, *Reflectarray antennas: Theory, designs, and applications*. John Wiley and Sons, 2018.

[8] W. Tang, M. Z. Chen, X. Chen, J. Y. Dai, Y. Han, M. Di Renzo, Y. Zeng, S. Jin, Q. Cheng, and T. J. Cui, "Wireless communications with reconfigurable intelligent surface: Path loss modeling and experimental measurement," *IEEE Trans. Wireless Commun.*, vol. 20, no. 1, pp. 421–439, Sept. 2021.

[9] J. Lan, J. Sang, M. Zhou, B. Gao, S. Meng, X. Li, W. Tang, S. Jin, Q. Cheng, T. J. Cui, and E. Basar, "Measurement and characteristic analysis of RIS-assisted wireless communication channels in sub-6 GHz outdoor scenarios," in *Proc. VTC'23*, Florence, Italy, Jun. 2023, pp. 1–6.

[10] J. Sang, M. Zhou, J. Lan, B. Gao, W. Tang, X. Li, S. Jin, E. Basar, C. Li, Q. Cheng, and T. J. Cui, "Multi-scenario broadband channel measurement and modeling for sub-6 GHz RIS-assisted wireless communication systems," *IEEE Trans. Wireless Commun.*, vol. 23, no. 6, pp. 6312–6329, Jun. 2024.

[11] Y. Wang, Z. Lian, Y. Wang, Y. Su, B. Jin, and Z. Zhang, "Geometry-based UAV-MIMO channel model for intelligent reflecting surface-assisted communication systems," *IEEE Trans. Veh. Technol.*, vol. 73, no. 1, pp. 14–27, Jan. 2024.

[12] Z. Lian, Y. Su, Y. Wang, P. Ji, B. Jin, Z. Zhang, and Z. Xie, "A novel geometry-based 3-D wideband channel model and capacity analysis for IRS-assisted UAV communication systems," *IEEE Trans. Wireless Commun.*, vol. 22, no. 8, pp. 5502–5517, Jan. 2023.

[13] G. Sun, R. He, J. An, B. Ai, Y. Song, Y. Niu, G. Wang, and C. Yuen, "Geometric-based channel modeling and analysis for double-RIS aided vehicle-to-vehicle communication systems," *IEEE Internet Things J.*, vol. 11, no. 10, pp. 18 888–18 901, May 2024.

[14] B. Xiong, Z. Zhang, H. Jiang, H. Zhang, J. Zhang, L. Wu, and J. Dang, "A statistical MIMO channel model for reconfigurable intelligent surface assisted wireless communications," *IEEE Trans. Commun.*, vol. 70, no. 2, pp. 1360–1375, Dec. 2022.

[15] Y. Yuan, R. He, B. Ai, Y. Niu, M. Yang, G. Wang, R. Chen, Y. Li, J. Li, J. Ding, and Z. Zhong, "A 3D geometry-based reconfigurable intelligent surfaces-assisted mmWave channel model for high-speed train communications," *IEEE Trans. Veh. Technol.*, vol. 73, no. 2, pp. 1524–1539, Feb. 2024.

[16] H. Jiang, B. Xiong, H. Zhang, and E. Basar, "Physics-based 3D end-to-end modeling for double-RIS assisted non-stationary UAV-to-ground communication channels," *IEEE Trans. Commun.*, vol. 71, no. 7, pp. 4247–4261, Jul. 2023.

[17] *Study on Channel Model for Frequencies From 0.5 to 100 GHz*, document 3GPP TR 38.901, Version 16.1.0, Release 16, Dec. 2019.

[18] R. C. Ferreira, M. S. P. Facina, F. A. P. De Figueiredo, G. Fraidenraich, and E. R. De Lima, "Bit error probability for large intelligent surfaces under double-Nakagami fading channels," *IEEE Open J. Commun. Soc.*, vol. 1, pp. 750–759, May 2020.

[19] Y. Sun, C.-X. Wang, J. Huang, and J. Wang, "A 3D non-stationary channel model for 6G wireless systems employing intelligent reflecting surfaces with practical phase shifts," *IEEE Trans. Cognit. Commun. Netw.*, vol. 7, no. 2, pp. 496–510, Jun. 2021.

[20] E. Basar and I. Yildirim, "Reconfigurable intelligent surfaces for future wireless networks: A channel modeling perspective," *IEEE Wireless Commun.*, vol. 28, no. 3, pp. 108–114, Apr. 2021.

[21] M. Tatar Mamaghani and Y. Hong, "Aerial intelligent reflecting surface-enabled terahertz covert communications in beyond-5G internet of things," *IEEE Internet Things J.*, vol. 9, no. 19, pp. 19012–19033, Mar. 2022.

[22] H. Lu, Y. Zeng, S. Jin, and R. Zhang, "Aerial intelligent reflecting surface: Joint placement and passive beamforming design with 3D beam flattening," *IEEE Trans. Wireless Commun.*, vol. 20, no. 7, pp. 4128–4143, Feb. 2021.

[23] Y. Pan, K. Wang, C. Pan, H. Zhu, and J. Wang, "UAV-assisted and intelligent reflecting surfaces-supported terahertz communications," *IEEE Wireless Commun. Lett.*, vol. 10, no. 6, pp. 1256–1260, Mar. 2021.

[24] Z. Ma, B. Ai, R. He, H. Mi, M. Yang, N. Wang, Z. Zhong, and W. Fan, "Modeling and analysis of MIMO multipath channels with aerial intelligent reflecting surface," *IEEE J. Sel. Areas Commun.*, vol. 40, no. 10, pp. 3027–3040, Aug. 2022.

[25] X. Wu, J. Bian, Z. Wang *et al.*, "A three-dimensional wideband mmWave multiple-input multiple-output channel model for aerial reconfigurable intelligent surface-assisted communication systems," *Int. J. Commun. Syst.*, vol. 37, no. 6, pp. 1–19, Dec. 2024.

[26] V. Jamali, W. Ghanem, R. Schober, and H. V. Poor, "Impact of channel models on performance characterization of RIS-assisted wireless systems," in *Proc. EuCAP'23*, Florence, Italy, Mar. 2023, pp. 1–5.

[27] M. Gapeyenko, D. Moltchanov, S. Andreev, and R. W. Heath, "Line-of-sight probability for mmWave-based UAV communications in 3D urban grid deployments," *IEEE Trans. Wireless Commun.*, vol. 20, no. 10, pp. 6566–6579, Apr. 2021.

[28] Z. Wang, J. Bian, C.-X. Wang, Y. Liu, and J. Tian, "Aerial reconfigurable intelligent surface-assisted channel modeling incorporating the effect of UAV fluctuations," *IEEE Commun. Lett.*, Jul. 2024.

[29] ITU-R, "P.1410-6: Propagation data and prediction methods required for the design of terrestrial broadband radio access systems operating in a frequency range from 3 to 60 GHz," Tech. Rep., Aug. 2023.

[30] H. Ni, Q. Zhu, B. Hua, K. Mao, Y. Pan, F. Ali, W. Zhong, and X. Chen, "Path loss and shadowing for UAV-to-ground UWB channels incorporating the effects of built-up areas and airframe," *IEEE trans. Intell. Transp. Syst.*, pp. 1–12, 2024, in press.

[31] K. Mao, Q. Zhu, Y. Qiu, X. Liu, M. Song, W. Fan, A. B. J. Kokkeler, and Y. Miao, "A UAV-aided real-time channel sounder for highly dynamic nonstationary A2G scenarios," *IEEE Trans. Instrum. Meas.*, vol. 72, pp. 1–15, Aug. 2023.

[32] Q. Qin, Z. Zhong, X. Gao, J. Zhao, C. Li, L. Fan, and Z. Jiang, "The measurement-based intelligent reflecting surfaces path loss model," in *Proc. EuCAP'22, Madrid, Spain*, Mar. 2022, pp. 1–5.

[33] Y. Zhang, S. Jyoti, C. R. Anderson, D. J. Love, N. Michelusi, A. Sprintson, and J. V. Krogmeier, "28-GHz channel measurements and modeling for suburban environments," in *Proc. IEEE ICC'18*, Kansas City, USA, May 2018, pp. 1–6.

[34] G. R. Maccartney, T. S. Rappaport, M. K. Samimi, and S. Sun, "Millimeter-wave omnidirectional path loss data for small cell 5G channel modeling," *IEEE Access*, vol. 3, pp. 1573–1580, Aug. 2015.

[35] B. Xiong, Z. Zhang, C. Pan, and J. Wang, "Performance analysis of aerial RIS auxiliary mmWave mobile communications with UAV fluctuation," *IEEE Wireless Commun. Lett.*, vol. 13, no. 4, pp. 1183–1187, Apr. 2024.

[36] Z. Lian, Z. Lin, Y. Wang, Y. Su, L. Ling, and H. Luo, "A novel beam channel model for AIRS-assisted mobile-to-mobile communication systems," *IEEE Internet Things J.*, vol. 11, no. 7, pp. 12 307–12 318, Apr. 2024.

[37] E. Basar, I. Yildirim, and F. Kilinc, "Indoor and outdoor physical channel modeling and efficient positioning for reconfigurable intelligent surfaces in mmWave bands," *IEEE Trans. Commun.*, vol. 69, no. 12, pp. 8600–8611, Sept. 2021.

[38] M. A. ElMossallamy, H. Zhang, L. Song, K. G. Seddik, Z. Han, and G. Y. Li, "Reconfigurable intelligent surfaces for wireless communications: Principles, challenges, and opportunities," *IEEE Trans. Cognit. Commun. Networking*, vol. 6, no. 3, pp. 990–1002, May 2020.

[39] S. Silver, *Microwave Antenna Theory and Design*. London: Institution of Engineering and Technology (IET), 1984.

[40] E. Björnson and L. Sanguinetti, "Rayleigh fading modeling and channel hardening for reconfigurable intelligent surfaces," *IEEE Wireless Commun. Lett.*, vol. 10, no. 4, pp. 830–834, Dec. 2021.